

# Uniform shear flow in dissipative gases. Computer simulations of inelastic hard spheres and (frictional) elastic hard spheres

Antonio Astillero\*

*Departamento de Informática, Centro Universitario de Mérida,  
Universidad de Extremadura, E-06800 Mérida, Badajoz, Spain*

Andrés Santos†

*Departamento de Física, Universidad de Extremadura, E-06071 Badajoz, Spain*

(Dated: September 30, 2018)

In the preceding paper (cond-mat/0405252), we have conjectured that the main transport properties of a dilute gas of inelastic hard spheres (IHS) can be satisfactorily captured by an equivalent gas of elastic hard spheres (EHS), provided that the latter are under the action of an effective drag force and their collision rate is reduced by a factor  $(1 + \alpha)/2$  (where  $\alpha$  is the constant coefficient of normal restitution). In this paper we test the above expectation in a paradigmatic nonequilibrium state, namely the simple or uniform shear flow, by performing Monte Carlo computer simulations of the Boltzmann equation for both classes of dissipative gases with a dissipation range  $0.5 \leq \alpha \leq 0.95$  and two values of the imposed shear rate  $a$ . It is observed that the evolution toward the steady state proceeds in two stages: a short kinetic stage (strongly dependent on the initial preparation of the system) followed by a slower hydrodynamic regime that becomes increasingly less dependent on the initial state. Once conveniently scaled, the intrinsic quantities in the hydrodynamic regime depend on time, at a given value of  $\alpha$ , only through the reduced shear rate  $a^*(t) \propto a/\sqrt{T(t)}$ , until a steady state, independent of the imposed shear rate and of the initial preparation, is reached. The distortion of the steady-state velocity distribution from the local equilibrium state is measured by the shear stress, the normal stress differences, the cooling rate, the fourth and sixth cumulants, and the shape of the distribution itself. In particular, the simulation results seem to be consistent with an exponential overpopulation of the high-velocity tail. These properties are common to both the IHS and EHS systems. In addition, the EHS results are in general hardly distinguishable from the IHS ones if  $\alpha \gtrsim 0.7$ , so that the distinct signature of the IHS gas (higher anisotropy and overpopulation) only manifests itself at relatively high dissipations.

PACS numbers: 45.70.Mg, 05.20.Dd, 05.60.-k, 51.10.+y

## I. INTRODUCTION

A granular gas in the rapid flow regime is usually modeled as a system of smooth inelastic hard spheres with a constant coefficient of normal restitution  $\alpha$ . The key ingredient of this minimal model is that energy is not conserved in collisions: in every binary collision, an amount of energy proportional to  $1 - \alpha^2$  is transferred to the internal degrees of freedom and thus it is lost as translational kinetic energy. Therefore, the gas “cools” down and the granular temperature monotonically decreases in time unless energy is externally injected into the system to compensate for the collisional loss. If this energy injection takes place through the boundaries (e.g., vibrating walls, thermal walls, sliding walls, ...) a nonequilibrium steady state can be reached characterized by strong spatial gradients in basic average quantities, such as density, mean velocity, or temperature. Kinetic theory tools can be straightforwardly extended to granular gases and, in

particular, the Boltzmann and Enskog kinetic equations have been formulated for inelastic collisions [1, 2, 3].

In the preceding paper [4], we have suggested that the nonequilibrium transport properties of a genuine gas of inelastic hard spheres (IHS) can be accounted for, to some extent, by an “equivalent” gas of elastic hard spheres (EHS). This requires the inclusion of two basic points. First, the EHS are assumed to feel the action of a drag force with a friction coefficient that mimics the collisional cooling rate of the true IHS gas. This guarantees that the local energy balance is approximately the same in both systems. Second, the collision rate of the EHS gas must be decreased by a factor  $\beta(\alpha)$  with respect to that of the IHS gas at the same (local) density and temperature. This can be interpreted under the assumption that, while the EHS have the same mass  $m$  as the IHS, they have a diameter  $\sigma' = \beta^{1/2}\sigma$  (where henceforth we are restricting ourselves to three-dimensional systems) smaller than the diameter  $\sigma$  of the IHS. Comparison between some basic collision integrals for IHS and EHS suggests the simple choice  $\beta = \frac{1}{2}(1 + \alpha)$  [4] to optimize the agreement between both descriptions.

The aim of this paper is two-fold. First, we want to assess to what extent the EHS gas succeeds in mimicking the transport properties and other quantities of the IHS gas by choosing the most widely studied nonequilibrium

---

\*Electronic address: aavivas@unex.es;  
URL: <http://www.unex.es/eweb/fisteor/antonio/>

†Electronic address: andres@unex.es;  
URL: <http://www.unex.es/eweb/fisteor/andres/>

state, namely the simple or uniform shear flow (USF). Since the USF state is intrinsically non-Newtonian [5, 6], it provides an interesting test case to check whether or not the IHS and EHS gases behave similarly in extreme situations far from equilibrium. As we will see, it turns out that most of the nonequilibrium properties of both types of system are practically indistinguishable for degrees of dissipation as large as  $\alpha \approx 0.7$ . For higher dissipations, the agreement is still at least semi-quantitative. The second goal of the paper is to carry out a rather extensive study of the most relevant properties of the USF in dissipative gases. This study includes the unsteady or transient regime (usually neglected in previous studies), which can be decomposed into a *kinetic* stage followed by a *hydrodynamic* stage. In the steady state we pay special attention not only to the rheological properties, but also to the velocity cumulants and to the distribution function itself.

The paper is organized as follows. The Boltzmann equation for both types of system, IHS and EHS, is briefly recalled in Sec. II, where also part of the notation is introduced. This is followed in Sec. III by a description of the USF and of the main quantities of interest. Section IV is devoted to some details of the numerical simulation method employed to solve the Boltzmann equation for each class of systems. The most important part of the paper is contained in Sec. V, where the results for the transient and steady-state problems are presented and discussed. When possible, the simulation data are also compared with predictions from a simple kinetic model [4, 7]. The paper is closed by some concluding remarks in Sec. VI.

## II. BOLTZMANN EQUATION

In a kinetic theory description the relevant quantity is the one-particle velocity distribution function  $f(\mathbf{r}, \mathbf{v}; t)$ . Its first five moments define the number density

$$n(\mathbf{r}, t) = \int d\mathbf{v} f(\mathbf{r}, \mathbf{v}; t), \quad (2.1)$$

the nonequilibrium flow velocity

$$\mathbf{u}(\mathbf{r}, t) = \frac{1}{n(\mathbf{r}, t)} \int d\mathbf{v} \mathbf{v} f(\mathbf{r}, \mathbf{v}; t), \quad (2.2)$$

and the *granular* temperature

$$T(\mathbf{r}, t) = \frac{m}{3n(\mathbf{r}, t)} \int d\mathbf{v} V^2(\mathbf{r}, t) f(\mathbf{r}, \mathbf{v}; t), \quad (2.3)$$

where  $m$  is the mass of a particle and  $\mathbf{V}(\mathbf{r}, t) \equiv \mathbf{v} - \mathbf{u}(\mathbf{r}, t)$  is the peculiar velocity. The hydrostatic pressure  $p = nT$  is one third the trace of the pressure tensor  $\mathbf{P}$  defined as

$$\mathbf{P}(\mathbf{r}, t) = m \int d\mathbf{v} \mathbf{V}(\mathbf{r}, t) \mathbf{V}(\mathbf{r}, t) f(\mathbf{r}, \mathbf{v}; t). \quad (2.4)$$

### A. Inelastic hard spheres

The evolution of  $f$  in the low-density limit is governed by the Boltzmann equation. In the case of a gas of inelastic hard spheres (IHS), it reads [1, 2, 3]

$$(\partial_t + \mathbf{v} \cdot \nabla) f = J^{(\alpha)}[f, f], \quad (2.5)$$

where  $J^{(\alpha)}[f, f]$  is the Boltzmann collision operator

$$J^{(\alpha)}[f, f] = \sigma^2 \int d\mathbf{v}_1 \int d\hat{\boldsymbol{\sigma}} \Theta(\mathbf{g} \cdot \hat{\boldsymbol{\sigma}}) (\mathbf{g} \cdot \hat{\boldsymbol{\sigma}}) \times [\alpha^{-2} f(\mathbf{v}'') f(\mathbf{v}_1'') - f(\mathbf{v}) f(\mathbf{v}_1)], \quad (2.6)$$

the explicit dependence of  $f$  on  $\mathbf{r}$  and  $t$  having been omitted. In Eq. (2.6),  $\sigma$  is the diameter of a sphere,  $\Theta$  is the Heaviside step function,  $\hat{\boldsymbol{\sigma}}$  is a unit vector directed along the centers of the two colliding spheres at contact,  $\mathbf{g} = \mathbf{v} - \mathbf{v}_1$  is the relative velocity, and  $\alpha$  is the coefficient of normal restitution. The pre-collisional or restituting velocities  $\mathbf{v}''$  and  $\mathbf{v}_1''$  are given by

$$\mathbf{v}'' = \mathbf{v} - \frac{1 + \alpha}{2\alpha} (\mathbf{g} \cdot \hat{\boldsymbol{\sigma}}) \hat{\boldsymbol{\sigma}}, \quad \mathbf{v}_1'' = \mathbf{v}_1 + \frac{1 + \alpha}{2\alpha} (\mathbf{g} \cdot \hat{\boldsymbol{\sigma}}) \hat{\boldsymbol{\sigma}}, \quad (2.7)$$

while the direct collision rule is

$$\mathbf{v}' = \mathbf{v} - \frac{1 + \alpha}{2} (\mathbf{g} \cdot \hat{\boldsymbol{\sigma}}) \hat{\boldsymbol{\sigma}}, \quad \mathbf{v}_1' = \mathbf{v}_1 + \frac{1 + \alpha}{2} (\mathbf{g} \cdot \hat{\boldsymbol{\sigma}}) \hat{\boldsymbol{\sigma}}. \quad (2.8)$$

The inelasticity of collisions contributes to a decrease of the granular temperature  $T(t)$ , i.e.,

$$\frac{m}{3n} \int d\mathbf{v} V^2 J^{(\alpha)}[f, f] = -\zeta T, \quad (2.9)$$

where  $\zeta$  is the *cooling rate*. By standard manipulations of the collision operator, the cooling rate can be written as [2, 7]

$$\zeta = \frac{\tau^{-1}}{48} \left(\frac{m}{T}\right)^{3/2} \langle V_{12}^3 \rangle (1 - \alpha^2), \quad (2.10)$$

where

$$\langle V_{12}^3 \rangle = \frac{1}{n^2} \int d\mathbf{v}_1 \int d\mathbf{v}_2 |\mathbf{v}_1 - \mathbf{v}_2|^3 f(\mathbf{v}_1) f(\mathbf{v}_2) \quad (2.11)$$

is the (local) average value of the cube of the relative speed and

$$\tau = \frac{\lambda}{\sqrt{2T/m}} \quad (2.12)$$

is a (local) characteristic time,

$$\lambda = \left(\sqrt{2\pi n \sigma^2}\right)^{-1} \quad (2.13)$$

being the (local) mean free path. Note that the cooling rate  $\zeta$  is a *nonlinear functional* of the distribution function  $f$  through the average  $\langle V_{12}^3 \rangle$  and cannot be explicitly

evaluated without the knowledge of  $f$ . Nevertheless, a simple *estimate* is obtained from Eq. (2.11) by replacing the actual distribution function  $f$  by the *local equilibrium* distribution

$$f_0(\mathbf{v}) = n(m/2\pi T)^{3/2} \exp(-mV^2/2T). \quad (2.14)$$

In that case,

$$\langle V_{12}^3 \rangle \rightarrow \langle V_{12}^3 \rangle_0 = \frac{32}{\sqrt{\pi}} \left( \frac{T}{m} \right)^{3/2}. \quad (2.15)$$

Insertion of this approximation into Eq. (2.10) yields the *local equilibrium* cooling rate [7, 8]

$$\zeta_0 = \frac{2\tau^{-1}}{3\sqrt{\pi}}(1 - \alpha^2). \quad (2.16)$$

This local equilibrium estimate is still a functional of  $f$ , but only through the local density and temperature, i.e.,  $\zeta_0 \propto nT^{1/2}$ . In addition, its dependence on inelasticity is simply  $\zeta_0 \propto 1 - \alpha^2$ .

The characteristic time  $\tau$  defined by Eqs. (2.12) and (2.13) is of the order of the (local equilibrium) mean free time  $\tau_{\text{mft}}$ , namely

$$\tau_{\text{mft}} = \frac{\lambda}{\langle V \rangle_0} = \frac{\sqrt{\pi}}{2} \tau, \quad (2.17)$$

where in the last step we have taken into account that the mean (peculiar) speed is  $\langle V \rangle \rightarrow \langle V \rangle_0 = \sqrt{8T/\pi m}$  in the local equilibrium approximation. It is also convenient to introduce a characteristic time  $\tau_\eta$  associated with the momentum transfer or viscosity. Its expression is

$$\tau_\eta = \frac{\eta_0}{nT} = 1.016 \frac{5\sqrt{\pi}}{8} \tau, \quad (2.18)$$

where  $\eta_0 = 1.016 \times 5\sqrt{mT/\pi}/16\sigma^2$  is the Navier–Stokes shear viscosity in the elastic limit ( $\alpha \rightarrow 1$ ) [9]. Note that  $\tau_\eta/\tau \approx \tau/\tau_{\text{mft}} \approx 1.13$ .

### B. (Frictional) elastic hard spheres

Now we consider a dilute gas of elastic hard spheres (EHS) of the same mass  $m$  as the IHS but with a diameter  $\sigma' = [\beta(\alpha)]^{1/2}\sigma$  smaller than that of the IHS. As a consequence, the characteristic time  $\tau'$  and the mean free path  $\lambda'$  of the EHS gas are [10]

$$\tau' = \frac{\lambda'}{\sqrt{2T/m}}, \quad \lambda' = \frac{1}{\beta} \left( \sqrt{2}n\pi\sigma^2 \right)^{-1}. \quad (2.19)$$

Furthermore, we assume that the EHS are under the influence of a drag force  $\mathbf{F}_{\text{drag}} = -m\gamma(\alpha)\mathbf{V}$  with a friction constant  $\gamma(\alpha) = \frac{1}{2}\zeta_0(\alpha)$ , where  $\zeta_0(\alpha)$  is given by Eq. (2.16). Therefore, the Boltzmann equation for the (frictional) EHS gas is

$$\left( \partial_t + \mathbf{v} \cdot \nabla - \frac{\zeta_0}{2} \frac{\partial}{\partial \mathbf{v}} \cdot \mathbf{V} \right) f = \beta J^{(1)}[f, f], \quad (2.20)$$

where the elastic collision operator  $J^{(1)}[f, f]$  is given by Eq. (2.6) by setting  $\alpha = 1$  both explicitly and in the collision rule (2.7), but keeping the factor  $\sigma^2$ . Henceforth, when referring to the EHS system, we will always understand that the particles are frictional, in the sense that the external force  $\mathbf{F}_{\text{drag}}$  is acting on them [11].

Friction produces in the EHS gas a cooling effect characterized by the rate  $\zeta_0(\alpha)$ . This is intended to mimic the cooling effect in the IHS gas due to the collisional inelasticity, which is characterized by the rate  $\zeta(\alpha)$  given by Eq. (2.10). Both cooling rates are quantitatively close each other as long as the density and temperature are similar in both systems and (2.15) is a good approximation. In principle, we could consider a friction constant  $\gamma = \frac{1}{2}\zeta_0\langle V_{12}^3 \rangle / \langle V_{12}^3 \rangle_0$ , so that the cooling rate of the EHS would be the same functional of  $f$  as in the IHS case. However, this would complicate excessively the EHS model without a correlated gain in accuracy, as we will see in Sec. V C.

The parameter  $\beta(\alpha) = (\sigma'/\sigma)^2$  can be adjusted to optimize the agreement between the physically most relevant integrals involving  $J^{(\alpha)}[f, f]$  and  $\beta J^{(1)}[f, f] + \frac{1}{2}\zeta_0 \partial_{\mathbf{v}} \cdot (\mathbf{V}f)$ . The simplest choice is [4]

$$\beta = \frac{1 + \alpha}{2}. \quad (2.21)$$

Of course, the IHS and EHS gases described by the Boltzmann equations (2.5) and (2.20), respectively, are intrinsically different. However, it might be possible that the main transport properties, which are measured by low-velocity moments such as in Eqs. (2.1)–(2.4), are similar in both systems. As said in Sec. I, one of the goals of this paper is to check this expectation in the case of the uniform shear flow [12].

## III. UNIFORM SHEAR FLOW

The uniform (or simple) shear flow (USF) is perhaps the nonequilibrium state most widely studied, both for granular [6, 13, 14, 15, 16, 17, 18, 19, 20, 21, 22, 23, 24, 25, 26, 27, 28, 29, 30, 31, 32, 33, 34, 35, 36, 37, 38, 39, 40] and conventional [41] gases. In this state the gas is enclosed between two infinite parallel planes located at  $y = -L/2$  and  $y = +L/2$  and in relative motion with velocities  $-U/2$  and  $+U/2$ , respectively, along the  $x$ -direction. The planes do not represent realistic bounding walls, in contrast to what happens in the true Couette flow [42]. Instead, the planes represent virtual boundaries where the Lees–Edwards boundary conditions are applied [43, 44]: every time a particle crosses one of the planes with a given velocity  $\mathbf{v}$ , it is reentered at once through the opposite plane with a velocity  $\mathbf{v}'$  such that the relative velocity with respect to the plane is preserved, i.e.,  $\mathbf{v}' = \mathbf{v} - U\hat{\mathbf{x}}$  if the particle is reentered through the bottom plate and  $\mathbf{v}' = \mathbf{v} + U\hat{\mathbf{x}}$  if it is reentered through the top plate. In terms of the velocity distribution function, these generalized periodic boundary

conditions read

$$f(y = \pm L/2, \mathbf{v}; t) = f(y = \mp L/2, \mathbf{v} \mp U\hat{\mathbf{x}}; t). \quad (3.1)$$

This process injects energy into the system. Suppose a particle with a velocity  $\mathbf{v}$  crosses the top plane (i.e.,  $v_y > 0$ ); it is then transferred to the bottom plane with a new velocity  $\mathbf{v}' = \mathbf{v} - U\hat{\mathbf{x}}$ . The change in kinetic energy is therefore proportional to  $v'^2 - v^2 = 2U(U/2 - v_x)$ , which is positive (negative) if  $v_x < U/2$  ( $v_x > U/2$ ). Thus, some particles gain energy while other particles lose energy through the boundary conditions. On the other hand, the shearing motion tends to produce a negative shear stress ( $P_{xy} < 0$ ), so that particles moving upward near the top wall preferentially have  $v_x - U/2 < 0$ . Therefore,  $v'^2 - v^2 > 0$  on average. This *viscous heating* effect tends to increase the temperature, in opposition to the cooling effect due to the inelasticity of collisions (in the IHS case) or to the drag force (in the EHS case).

Starting from a given initial condition  $f(\mathbf{r}, \mathbf{v}; 0)$ , and after a certain transient regime, the system is expected to reach a nonequilibrium steady state where the above heating and cooling effects cancel each other. By symmetry reasons, this steady state is characterized by uniform density and temperature, and by a *linear* velocity profile  $\mathbf{u}(\mathbf{r}) = ay\hat{\mathbf{x}}$ , where  $a = U/L$  represents the imposed shear rate. More generally, the steady distribution function becomes *uniform* when the velocities of the particles are referred to the Lagrangian frame of reference co-moving with the flow velocity [44]:

$$f(\mathbf{r}, \mathbf{v}) \rightarrow f(\mathbf{V}), \quad \mathbf{V} = \mathbf{v} - ay\hat{\mathbf{x}}. \quad (3.2)$$

If the initial distribution function  $f(\mathbf{r}, \mathbf{v}; 0)$  depends on space only through the coordinate  $y$  normal to the plates, this property is maintained by the Boltzmann equations (2.5) and (2.20), so that one can make

$$\mathbf{v} \cdot \nabla \rightarrow v_y \frac{\partial}{\partial y}. \quad (3.3)$$

Furthermore, if  $f(\mathbf{r}, \mathbf{v}; 0)$  is consistent with the symmetry property (3.2), again this is maintained by the Boltzmann equations (2.5) and (2.20), what implies that

$$\mathbf{v} \cdot \nabla \rightarrow -aV_y \frac{\partial}{\partial V_x}. \quad (3.4)$$

In this latter situation, Eqs. (2.5) and (2.20) become spatially homogeneous equations since, in agreement with Eq. (3.4), the effect of convection is played by the non-conservative *inertial* force  $\mathbf{F}_{\text{shear}} = -maV_y\hat{\mathbf{x}}$ . In what follows, we will refer to the transient solution of Eqs. (2.5) and (2.20) with the replacement (3.4) as the *homogeneous* transient problem.

On the other hand, if the initial distribution depends spatially on  $y$  only but does not become uniform under the transformation (3.2), then the replacement (3.3) is valid but (3.4) is not. In that case, Eqs. (2.5) and (2.20) cannot be made equivalent to uniform equations

and their transient solutions define the *inhomogeneous* transient problem.

For the inhomogeneous transient problem we will consider two different initial states. The first one is the *equilibrium* state

$$f(\mathbf{r}, \mathbf{v}; 0) = \bar{n} \left( \frac{m}{2\pi T^0} \right)^{3/2} \exp \left( -\frac{mv^2}{2T^0} \right), \quad (3.5)$$

where  $\bar{n}$  and  $T^0$  are constants [45]. The gas is initially at rest (in the laboratory or Eulerian frame), but almost immediately the Lees–Edwards boundary conditions produce fluid motion near the walls, this motion being subsequently propagated to the rest of the system through free streaming and collisions. Eventually the flow velocity reaches the linear profile  $u_x(y) = ay$ . The transient period from  $u_x = 0$  to  $u_x = ay$  induces inhomogeneities in the density and temperature profiles, even though these quantities are initially uniform. As a second choice for the initial state we will take the distribution

$$f(\mathbf{r}, \mathbf{v}; 0) = \frac{n^0(y)}{4\pi V^0{}^2} \delta(|\mathbf{v} - \mathbf{u}^0(y)| - V^0), \quad (3.6)$$

where the initial density and velocity fields are

$$n^0(y) = \bar{n} \left( 1 + \frac{1}{2} \sin \frac{2\pi y}{L} \right), \quad (3.7)$$

$$\mathbf{u}^0(y) = U \left( \cos \frac{\pi y}{L} - \frac{2}{\pi} \right) \hat{\mathbf{x}}, \quad (3.8)$$

respectively, while the initial temperature  $T^0 = mV^0{}^2/3$  is uniform. The initial state (3.6) is very different from (3.5). Now, all the particles have the same magnitude  $V^0$  of the peculiar velocity. In addition, the initial density and flow velocity fields have the opposite symmetries to the ones imposed by the boundary conditions:  $n^0(-y) - \bar{n} = -[n^0(y) - \bar{n}]$  and  $\mathbf{u}^0(-y) = \mathbf{u}^0(y)$ . Therefore, high gradients are expected during the period of time before the boundary conditions establish a linear velocity profile and uniform density and temperature.

Regardless of the initial preparation of the system, conservation of the total number of particles implies that the average density coincides for all times with the initial value  $\bar{n}$ , i.e.,

$$\bar{n} = \frac{1}{L} \int_{-L/2}^{L/2} dy n(y, t). \quad (3.9)$$

However, the average temperature

$$\bar{T}(t) = \frac{1}{\bar{n}L} \int_{-L/2}^{L/2} dy n(y, t) T(y, t) \quad (3.10)$$

changes in time during the transient regime as a consequence of the competition between the dissipative cooling and the viscous heating.

A physically motivated way of measuring time is through the accumulated number of collisions per particle  $s(t)$  from the initial state to time  $t$ . In the local equilibrium approximation,  $s(t) = s_0(t)$ , where

$$s_0(t) = \frac{1}{2} \frac{2}{\sqrt{\pi}} \frac{1}{\bar{n}L} \int_0^t dt' \int_{-L/2}^{L/2} dy \frac{n(y, t')}{\tau(y, t')}. \quad (3.11)$$

Here, the local characteristic time  $\tau(y, t)$  is given by Eqs. (2.12) and (2.13). The factor  $\frac{1}{2}$  takes into account that two particles are involved in each collision, while the factor  $2/\sqrt{\pi}$  accounts for the relation  $\tau_{\text{mfp}}/\tau = \sqrt{\pi}/2$  [cf. Eq. (2.17)]. Note that  $s_0(t)$  is the (local equilibrium) number of collisions per particle of the IHS gas. The equivalent quantity for the EHS gas,  $s'_0(t)$ , is obtained from Eq. (3.11) by using the corresponding local characteristic time  $\tau'(y, t)$  defined by Eq. (2.19), instead of  $\tau(y, t)$ . In principle,  $s'_0(t) \neq \beta s_0(t)$  and, more generally,  $s'(t) \neq \beta s(t)$ , unless the density and temperature profiles, and their history, are the same in both systems [10]. We will come back to this point in Sec. VB.

In the analysis of the homogeneous transient problem, we will start from a *local equilibrium* initial state

$$f(\mathbf{r}, \mathbf{v}; 0) = \bar{n} \left( \frac{m}{2\pi T^0} \right)^{3/2} \exp \left[ -\frac{m}{2T^0} (\mathbf{v} - ay\hat{\mathbf{x}})^2 \right]. \quad (3.12)$$

In this case, the initial state is already uniform in the Lagrangian frame [cf. Eq. (3.2)], so that the velocity field is kept linear,  $u_x = ay$ , the density is constant,  $n = \bar{n}$ , and the temperature is uniform,  $T(y, t) = T(t)$ . Consequently, Eq. (3.11) becomes

$$s_0(t) = \frac{1}{\sqrt{\pi}} \int_0^t \frac{dt'}{\tau(t')}, \quad (3.13)$$

with a similar equation for  $s'_0(t)$  in the EHS case. Apart from the temperature  $T(t)$  and the elements  $P_{ij}(t)$  of the pressure tensor, we will also evaluate in the homogeneous transient problem the ratio  $\langle V_{12}^3 \rangle / \langle V_{12}^3 \rangle_0$ , as well as the fourth and sixth cumulants,

$$a_2 = \frac{\langle V^4 \rangle}{\langle V^4 \rangle_0} - 1, \quad a_3 = -\frac{\langle V^6 \rangle}{\langle V^6 \rangle_0} + 1 + 3a_2, \quad (3.14)$$

where  $\langle V^4 \rangle_0 = 15(T/m)^2$  and  $\langle V^6 \rangle_0 = 105(T/m)^3$ . We recall that the quantity  $\langle V_{12}^3 \rangle$  is directly related to the cooling rate of the IHS gas via Eq. (2.10), while the cumulants are measures of the deviation of the energy distribution from the Maxwellian. Those deviations will also be monitored through the ratios

$$R_\ell(t) = \frac{\int_{W_\ell}^{W_{\ell+1}} dV V^2 \int d\hat{\mathbf{V}} f(\mathbf{V}, t)}{\int_{W_\ell}^{W_{\ell+1}} dV V^2 \int d\hat{\mathbf{V}} f_0(\mathbf{V}, t)}, \quad \ell = 0, 1, 2, 3. \quad (3.15)$$

$R_\ell(t)$  is the fraction of particles that at time  $t$  move with a speed between  $W_\ell$  and  $W_{\ell+1}$ , divided by the same fraction in local equilibrium. We have taken for the integration limits the values  $W_\ell = C_\ell \sqrt{2T(t)/m}$  with  $C_0 = 0$ ,  $C_1 = 1$ ,  $C_2 = 2$ ,  $C_3 = 3$ , and  $C_4 = \infty$ .

In either transient problem, the final steady-state temperature  $T_s$  is smaller or larger than the initial value  $T^0$  depending on whether initially the dissipative cooling dominates or is dominated by the viscous heating, respectively. By dimensional analysis,  $T_s$  is proportional to  $a^2$  times a certain function of  $\alpha$ , being independent of  $T^0$ . Stated differently, the steady state is such that when the steady-state characteristic time  $\tau_s \propto T_s^{1/2}$  is nondimensionalized with the constant shear rate  $a$ , then it becomes a function of  $\alpha$  only. More generally, the *reduced* steady-state velocity distribution function

$$f_s^*(\mathbf{C}) = \frac{1}{n} \left( \frac{2T_s}{m} \right)^{3/2} f_s(\mathbf{V}), \quad \mathbf{C} = \frac{\mathbf{V}}{\sqrt{2T_s/m}}, \quad (3.16)$$

depends on  $\alpha$  but is independent of the shear rate  $a$  and the initial preparation of the system. Owing to the symmetry properties of the USF,

$$f_s^*(C_x, C_y, C_z) = f_s^*(C_x, C_y, -C_z) = f_s^*(-C_x, -C_y, C_z). \quad (3.17)$$

Since  $f_s^*(\mathbf{C})$  depends on the three velocity components in a non-trivial way, it is difficult to visualize it, so that it is convenient to consider the following *marginal* distributions:

$$g_x^{(\pm)}(C_x) = \int_{-\infty}^{\infty} dC_z \int_{-\infty}^{\infty} dC_y \Theta(\pm C_y) f_s^*(\mathbf{C}), \quad (3.18)$$

$$g_y^{(\pm)}(C_y) = \int_{-\infty}^{\infty} dC_z \int_{-\infty}^{\infty} dC_x \Theta(\pm C_x) f_s^*(\mathbf{C}), \quad (3.19)$$

$$F(C) = C^2 \int d\hat{\mathbf{C}} f_s^*(\mathbf{C}). \quad (3.20)$$

The function  $g_x^{(+)}(C_x)$  is the distribution of the  $x$ -component of the velocity of those particles moving upward (i.e., with  $C_y > 0$ ). The functions  $g_x^{(-)}(C_x)$ ,  $g_y^{(+)}(C_y)$ , and  $g_y^{(-)}(C_y)$  have a similar meaning. The symmetry properties (3.17) imply that

$$g_x^{(+)}(C_x) = g_x^{(-)}(-C_x), \quad g_y^{(+)}(C_y) = g_y^{(-)}(-C_y). \quad (3.21)$$

While the functions (3.18) and (3.19) provide information about the anisotropy of the state,  $F(C)$  is the probability distribution function of the magnitude of the peculiar velocity (in units of the thermal speed), regardless of its orientation.

#### IV. MONTE CARLO SIMULATIONS

We have solved numerically the Boltzmann equation (2.5) for the IHS system and the Boltzmann equation (2.20) for the EHS system by means of the Direct Simulation Monte Carlo (DSMC) method [46, 47, 48]. For the sake of completeness, we give below some details about the application of this method to our problem.

### A. Inhomogeneous transient problem

The USF has been implemented in the inhomogeneous transient problem by applying the Lees–Edwards boundary conditions (3.1), using the form (3.3) for the convection operator, and starting from the initial distribution (3.5) or (3.6). The separation between the boundaries has been taken as  $L = 2.5\lambda^0$  and the shear rate has been fixed at  $a\tau^0 = 4$ , where

$$\lambda^0 = \left(\sqrt{2\pi\bar{n}\sigma^2}\right)^{-1}, \quad \tau^0 = \frac{\lambda^0}{\sqrt{2T^0/m}} \quad (4.1)$$

are the initial (global) mean free path and characteristic time, respectively, of the IHS gas. The coefficient of restitution for the IHS has been taken as  $\alpha = 0.9$ . This same value has been taken in the EHS case for the friction constant  $\gamma = \frac{1}{2}\zeta_0$  and the factor  $\beta$ , as given by Eqs. (2.16) and (2.21), respectively.

According to the DSMC method [46, 47], the system is split into  $M$  layers of width  $\delta y = L/M$ . The velocity distribution function is represented by the positions  $\{y_i(t)\}$  and velocities  $\{\mathbf{v}_i(t)\}$  of a set of  $N$  simulated particles:

$$f(y, \mathbf{v}; t) \rightarrow \frac{1}{A} \sum_{i=1}^N \delta(y - y_i(t)) \delta(\mathbf{v} - \mathbf{v}_i(t)), \quad (4.2)$$

where  $A \equiv (N/L)/\bar{n}$  is a constant formally representing the area of a section of the system normal to the  $y$ -axis, so that  $A\delta y$  represents the volume of a layer. The number of particles inside a given layer  $I = 1, \dots, M$  is

$$N_I(t) = \sum_{i=1}^N \Theta_I(y_i(t)), \quad (4.3)$$

where  $\Theta_I(y)$  is the characteristic function of layer  $I$ , i.e.,  $\Theta_I(y) = 1$  if  $y$  belongs in  $I$  and  $\Theta_I(y) = 0$  otherwise. The (coarse-grained) number density, mean velocity, temperature, and pressure tensor of layer  $I$  are

$$n_I(t) = \frac{N_I(t)}{A\delta y}, \quad (4.4)$$

$$\mathbf{u}_I(t) = \frac{1}{N_I(t)} \sum_{i=1}^N \Theta_I(y_i(t)) \mathbf{v}_i(t), \quad (4.5)$$

$$T_I(t) = \frac{m}{3N_I(t)} \sum_{i=1}^N \Theta_I(y_i(t)) [\mathbf{v}_i(t) - \mathbf{u}_I(t)]^2, \quad (4.6)$$

$$P_I(t) = \frac{m}{A\delta y} \sum_{i=1}^N \Theta_I(y_i(t)) [\mathbf{v}_i(t) - \mathbf{u}_I(t)] [\mathbf{v}_i(t) - \mathbf{u}_I(t)]. \quad (4.7)$$

The average temperature and pressure tensor along the system are given by

$$\bar{T}(t) = \frac{1}{N} \sum_{I=1}^M N_I(t) T_I(t), \quad (4.8)$$

$$\bar{P}(t) = \frac{1}{M} \sum_{I=1}^M P_I(t). \quad (4.9)$$

The positions  $\{y_i(t)\}$  and velocities  $\{\mathbf{v}_i(t)\}$  of the particles are updated from time  $t$  to time  $t + \delta t$  in two stages:

1. *Free streaming.* In this stage,

$$y_i(t + \delta t) = y_i(t) + v_{iy}(t) \delta t. \quad (4.10)$$

If particle  $i$  crosses the top wall, i.e.,  $y_i(t + \delta t) > L/2$ , then its position and velocity are redefined as

$$y_i(t + \delta t) \rightarrow y_i(t + \delta t) - L, \quad \mathbf{v}_i(t) \rightarrow \mathbf{v}_i(t) - aL\hat{\mathbf{x}}. \quad (4.11)$$

A similar action takes place if particle  $i$  crosses the bottom wall, i.e.,  $y_i(t + \delta t) < -L/2$ .

In the case of IHS, the velocities are not modified during the free streaming stage. In the case of EHS, however, the action of the (local) friction force yields

$$\mathbf{v}_i(t + \delta t) = \mathbf{u}_I(t) + [\mathbf{v}_i(t) - \mathbf{u}_I(t)] e^{-\zeta_I(t)\delta t/2}. \quad (4.12)$$

Here,  $I$  is the layer where particle  $i$  sits at time  $t$  and  $\zeta_I(t) \propto n_I(t) \sqrt{T_I(t)} (1 - \alpha^2)$  is the coarse-grained version of the cooling rate  $\zeta_0$  defined by Eq. (2.16).

2. *Collision stage.* In this stage, a number

$$\mathcal{N}_I = \frac{N_I^2}{2\sqrt{2}N/M} \frac{w_I \delta t}{\lambda^0} \quad (\text{IHS}), \quad (4.13a)$$

$$\mathcal{N}'_I = \beta(\alpha) \frac{N_I^2}{2\sqrt{2}N/M} \frac{w_I \delta t}{\lambda^0} \quad (\text{EHS}) \quad (4.13b)$$

of candidate pairs are randomly selected for each layer  $I$ . In Eqs. (4.13),  $\lambda^0$  is given by Eq. (4.1) and  $w_I \propto \sqrt{T_I(t)}$  is an upper estimate of the maximum relative speed in layer  $I$ . The collision between each candidate pair  $ij$  is accepted with a probability equal to  $v_{ij}/w_I$ , where  $v_{ij}$  is the relative speed. If the collision is accepted, a direction  $\hat{\boldsymbol{\sigma}}$  is chosen at random with equiprobability and the velocities  $(\mathbf{v}_i, \mathbf{v}_j)$  are replaced by  $(\mathbf{v}'_i, \mathbf{v}'_j)$ , according to the collision rule (2.8) with  $\alpha < 1$  (IHS) or  $\alpha = 1$  (EHS).

The numerical values for the “technical” parameters are as follows. The layer thickness is  $\delta y = 0.05\lambda^0$  (i.e., the number of layers is  $M = 50$ ), the time step is  $\delta t = 10^{-3}\tau^0\sqrt{T^0/T}$  (so that it changes in time as the global characteristic time  $\bar{\tau} \propto 1/\sqrt{T}$  does), and the total number of particles is  $N = 10^4$ . The hydrodynamic quantities (density, flow velocity, temperature, and pressure tensor) are updated every 4 time steps and recorded every 160 time steps. Moreover, in order to improve the statistics, all the quantities are further averaged over three independent realizations of the system.

## B. Homogeneous transient problem

In the homogeneous transient problem the USF is implemented by working directly in the Lagrangian frame of reference [cf. Eq. (3.2)] and using (3.4). Since the resulting Boltzmann equation is uniform, only the (peculiar) velocities  $\{\mathbf{V}_i(t)\}$  of the  $N$  particles need to be stored and there is no need of splitting the system into cells or applying boundary conditions. The velocity distribution function is described by

$$f(\mathbf{V}; t) \rightarrow \frac{1}{\Omega} \sum_{i=1}^N \delta(\mathbf{V} - \mathbf{V}_i(t)), \quad (4.14)$$

where the constant  $\Omega \equiv N/\bar{n}$  formally represents the volume of the system. The temperature and the pressure tensor are evaluated as

$$T(t) = \frac{m}{3N} \sum_{i=1}^N V_i^2(t), \quad (4.15)$$

$$\mathbf{P}(t) = \frac{m}{\Omega} \sum_{i=1}^N \mathbf{V}_i(t)\mathbf{V}_i(t). \quad (4.16)$$

Analogously, the fourth and sixth cumulants of the distribution function [cf. Eq. (3.14)] and the ratios  $R_\ell$  [cf. Eq. (3.15)] are computed as

$$a_2(t) = \frac{m^2}{15T^2(t)} \frac{1}{N} \sum_{i=1}^N V_i^4(t) - 1, \quad (4.17)$$

$$a_3(t) = -\frac{m^3}{105T^3(t)} \frac{1}{N} \sum_{i=1}^N V_i^6(t) + 1 + 3a_2(t), \quad (4.18)$$

$$R_\ell(t) = \frac{N^{-1}}{\mathcal{P}(C_{\ell+1}) - \mathcal{P}(C_\ell)} \sum_{i=1}^N \Theta(V_i(t) - W_\ell(t)) \times \Theta(W_{\ell+1}(t) - V_i(t)), \quad (4.19)$$

where  $\mathcal{P}(x) = \text{erf}(x) - 2xe^{-x^2}/\sqrt{\pi}$ ,  $\text{erf}(x)$  being the error function. In order to evaluate the average of the cube

of the relative speed, a sample of  $N_p$  pairs is randomly chosen out of the total number  $N(N-1)/2$  of pairs, so that

$$\langle V_{12}^3 \rangle(t) = \frac{1}{N_p} \sum_{ij} |\mathbf{V}_i(t) - \mathbf{V}_j(t)|^3. \quad (4.20)$$

The velocity update  $\{\mathbf{V}_i(t)\} \rightarrow \{\mathbf{V}_i(t+\delta t)\}$  takes place again in two stages. In the free streaming stage for IHS, only the  $x$ -component of the velocities change according to the inertial force  $\mathbf{F}_{\text{shear}} = -maV_y\hat{\mathbf{x}}$ :

$$V_{ix}(t + \delta t) = V_{ix}(t) - V_{iy}(t)a\delta t. \quad (4.21)$$

On the other hand, for EHS we have the drag force  $\mathbf{F}_{\text{drag}} = -m(\zeta_0/2)\mathbf{V}$  in addition to  $\mathbf{F}_{\text{shear}}$ , so that

$$\begin{aligned} V_{ix}(t + \delta t) &= [V_{ix}(t) - V_{iy}(t)a\delta t] e^{-\zeta_0(t)\delta t/2}, \\ V_{iy,z}(t + \delta t) &= V_{iy,z}(t) e^{-\zeta_0(t)\delta t/2}, \end{aligned} \quad (4.22)$$

where  $\zeta_0(t)$  is given by Eq. (2.16) with  $\tau(t) = \lambda^0/\sqrt{2T(t)/m}$ .

The collision stage proceeds essentially as in the inhomogeneous case, except that formally the number of layers is  $M = 1$ . Therefore, a number

$$\mathcal{N} = \frac{N}{2\sqrt{2}} \frac{w\delta t}{\lambda^0} \quad (\text{IHS}), \quad (4.23a)$$

$$\mathcal{N}' = \beta(\alpha) \frac{N}{2\sqrt{2}} \frac{w\delta t}{\lambda^0} \quad (\text{EHS}) \quad (4.23b)$$

of candidate pairs are randomly selected out of the total number of pairs in the system,  $w \propto \sqrt{T(t)}$  being an upper estimate of the maximum value of the relative speeds  $\{V_{ij}\}$  in the whole system.

In the simulations of the homogeneous transient problem we have considered two values of the shear rate ( $a\tau^0 = 4$  and  $a\tau^0 = 0.1$ ) and ten values of the coefficient of restitution ( $\alpha = 0.5-0.95$  with a step  $\Delta\alpha = 0.05$ ), both for IHS and EHS. This gives a total of forty different systems simulated. However, in the discussion of the transient problem we will mainly report results corresponding to  $\alpha = 0.5$  and  $\alpha = 0.9$ . Once a steady state is reached, its properties are obtained by averaging the fluctuating simulation values over time. In the analysis of the steady state all the values  $\alpha = 0.5-0.95$  will be considered.

The technical parameters of the homogeneous simulations are  $\delta t = 10^{-3}\tau^0\sqrt{T^0/T}$  (the average quantities being updated every 4 time steps and recorded every 160 time steps),  $N = 10^4$ , and  $N_p = 2.5 \times 10^4$ .

## V. RESULTS

In this Section we present the simulation results obtained for the main physical quantities in the USF and compare the properties of the genuine IHS gas with those of the EHS gas.

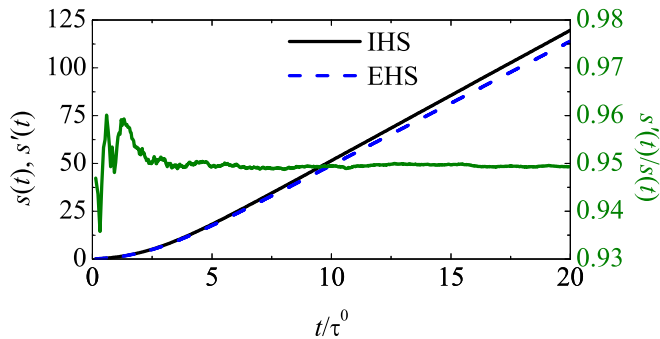


FIG. 1: (Color online) Accumulated number of collisions per particle as a function of time for IHS [ $s(t)$ , smooth solid line] and EHS [ $s'(t)$ , smooth dashed line] in the case  $\alpha = 0.9$ ,  $a\tau^0 = 4$ . The fluctuating solid line represents the ratio  $s'(t)/s(t)$ , the corresponding scale being that of the right vertical axis. The data have been obtained starting from the initial distribution function (3.5).

### A. Inhomogeneous transient problem

As said in Sec. IV, the initial distribution function in the inhomogeneous transient problem is either that of equilibrium, Eq. (3.5), or a strongly nonequilibrium one, Eq. (3.6). We have restricted ourselves to a coefficient of restitution  $\alpha = 0.9$  and a shear rate  $a = 4/\tau^0 = (4/0.95)/\tau^{0'}$ , where  $\tau^0$  and  $\tau^{0'} = \tau^0/\beta(\alpha) = \tau^0/0.95$  are the initial (global) characteristic times of the IHS and EHS gases, respectively. The values of  $a$  and  $\alpha$  are such that the viscous heating initially prevails over the dissipative cooling (either collisional or frictional) and so the temperature increases and the mean free time decreases.

We will mainly monitor the temporal evolution of the physical quantities by using an *internal* clock, namely the accumulated number of collisions per particle  $s(t)$  (IHS) and  $s'(t)$  (EHS), rather than the *external* time  $t$ . The quantities  $s(t)$  and  $s'(t)$  are computed directly by dividing the total number of accepted collisions until time  $t$  by the total number of particles; in general, they slightly differ from the local equilibrium values  $s_0(t)$  and  $s'_0(t)$  [cf. Eq. (3.11)]. Insofar as the velocity distribution function  $f(y, \mathbf{v}; t)$  is similar in both systems, one can expect that  $s'(t)/\beta(\alpha) \simeq s(t)$  [10]. Figure 1 shows  $s(t)$  and  $s'(t)$  as functions of time in the case of the initial state (3.5). The slopes of those curves are directly related to the respective temperatures; both slopes increase monotonically until becoming constant for  $t/\tau^0 \gtrsim 8$ . As expected, the accumulated number of collisions in the EHS gas up to any given time  $t$  is smaller than in the IHS gas, i.e.,  $s'(t) < s(t)$ . Figure 1 also shows the temporal evolution of the ratio  $s'(t)/s(t)$ . It fluctuates around  $\beta(\alpha) = 0.95$  up to  $t/\tau^0 \simeq 4$  and stays very close to 0.95 thereafter. This already provides an indirect validation of the practical equivalence between the profiles and history of the hydrodynamic quantities in both systems.

Figure 2 shows the velocity, density, and temperature

profiles at times  $t/\tau^0 = 0.13, 0.5, 1, 1.5,$  and  $2.0$ . The corresponding accumulated numbers of collisions per particle (for IHS) are  $s \simeq 0.08, 0.4, 1.1, 2.1,$  and  $3.4$  in the case of the initial distribution (3.5), and  $s \simeq 0.09, 0.5, 1.5, 2.8,$  and  $4.6$  in the case of the initial distribution (3.6). By time  $t/\tau^0 = 0.13$  only about 16–18% of particles have collided, so that the deviations from the initial profiles are essentially due to the boundary conditions. As a consequence, at  $t/\tau^0 = 0.13$  the flow velocity is almost the initial one everywhere except in the layers adjacent to the walls; moreover, those layers have a much larger temperature than the bulk, while the number density is still practically unchanged. As time advances, the more energetic particles near the boundaries travel inside the system and transfer part of their momentum and energy to the other particles by means of collisions. This produces a stretching of the shape of the velocity profile as well as a homogenization of temperature. The layers adjacent to the walls are first partially depopulated in favor of the central layers, but as the velocity profile becomes linear and the temperature becomes uniform, so does the density. In summary, Fig. 2 clearly shows that the hydrodynamic profiles freely evolve toward the characteristic profiles of the USF, regardless of the initial preparation of the system. It must be noted that, although the USF is known to be unstable with respect to excitations of sufficiently long wavelengths [19, 21, 23, 29], the size of the simulated systems ( $L = 2.5\lambda^0$ ) is small enough to suppress such an instability. As a matter of fact, a recent analysis from kinetic theory [49] shows that at  $\alpha = 0.9$  the instability does not appear unless  $L \gtrsim 25\lambda^0$ .

For the sake of clarity of the graphs, in the remainder of this Subsection we restrict ourselves to present simulation results obtained from the initial distribution (3.5). To monitor the time needed to establish a linear velocity profile and uniform density and temperature, we have followed the evolution of those quantities averaged over the four central layers ( $-2\delta y \leq y \leq 2\delta y$ ) and over the three top layers ( $L/2 - 3\delta y \leq y \leq L/2$ ). The results are displayed in Fig. 3. The flow velocity at  $y \approx 0$  fluctuates around zero, as expected by symmetry, whereas the velocity near the top wall monotonically increases (except for fluctuations) toward the wall velocity  $U/2$ . The maximum density difference appears after about one collision per particle, while the maximum temperature difference appears earlier at  $s \simeq 0.15$ . The characteristic hydrodynamic profiles of USF, i.e., linear velocity and uniform density and temperature, are reached approximately at  $s = 4$  (which corresponds to a “real” time  $t/\tau^0 \simeq 2.2$ ). From this time on, the evolution proceeds essentially as in the homogeneous transient problem.

In Figs. 2 and 3 we have scaled the local temperature  $T(y, t)$  with respect to its average value  $\bar{T}(t)$  in order to focus on the transient period toward uniformity. However, once the system becomes “homogeneous” [in the sense of Eq. (3.2)] at  $s \simeq 4$ , the temperature keeps evolving in time until the steady state is reached. This is observed in the top panel of Fig.

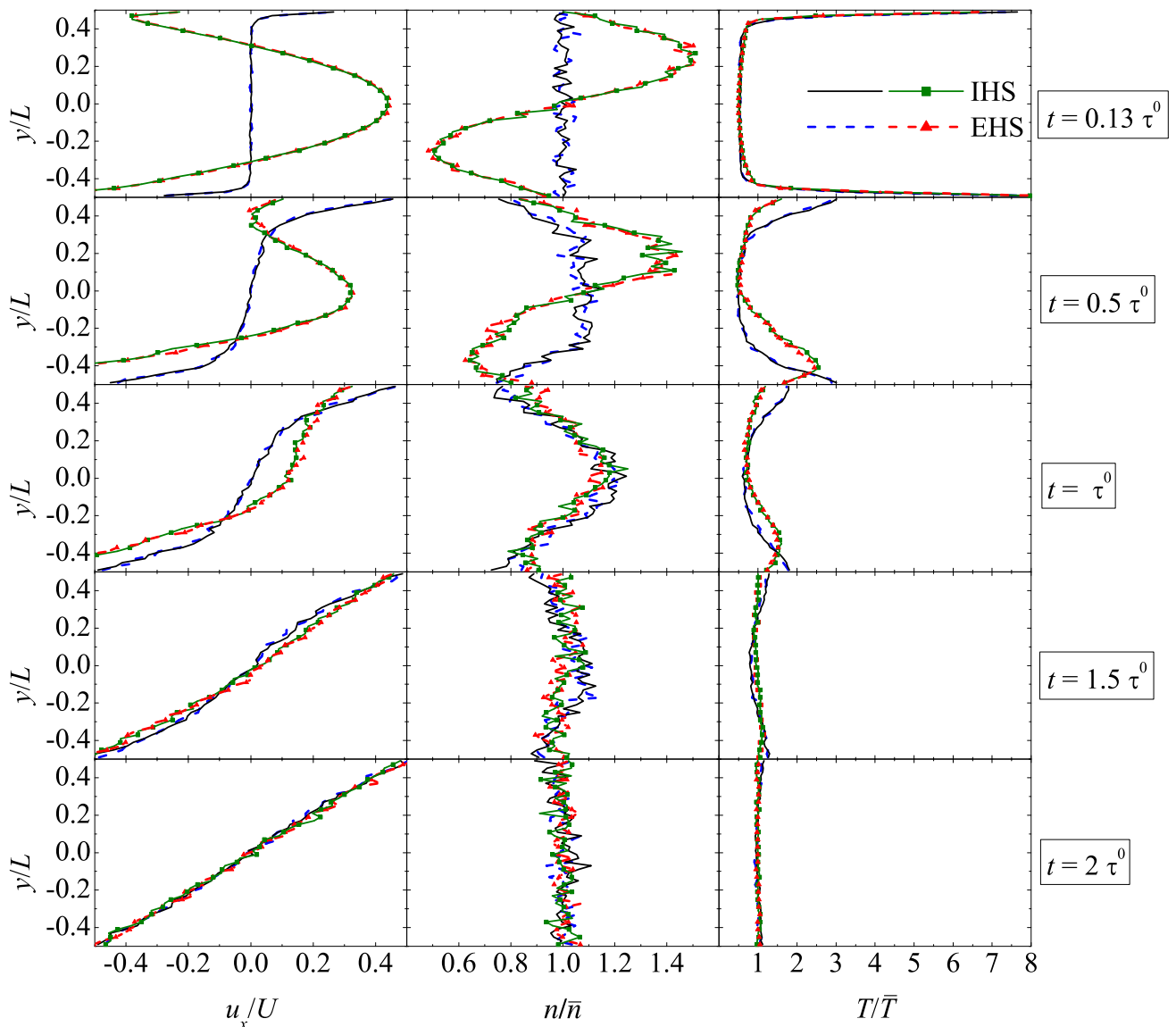


FIG. 2: (Color online) Hydrodynamic profiles for IHS (solid lines) and EHS (dashed lines) in the case  $\alpha = 0.9$ ,  $a\tau^0 = 4$ , at times  $t/\tau^0 = 0.13, 0.5, 1, 1.5$ , and  $2$ . The data have been obtained starting from the initial distribution function (3.5) (curves without symbols) or (3.6) (curves with symbols).

4, which shows the evolution of  $\bar{T}/T^0$ . We note that the total transient period is much longer than the duration of the inhomogeneous state. The temperature reaches a stationary value much larger than the initial one ( $\bar{T}_s/T^0 \simeq 147$ ) at  $s \simeq 50$  ( $t/\tau^0 \simeq 9.8$ ). Stationarity of temperature does not necessarily imply that the steady state has been reached since, in principle, the particles could redistribute their velocities along time without altering the mean kinetic energy. A strong indication that this is not actually the case is provided by the bottom panel of Fig. 4, which shows the evolution of the (reduced) shear stress  $-\bar{P}_{xy}/\bar{n}\bar{T}$  and the (reduced) normal stress difference  $(\bar{P}_{xx} - \bar{P}_{yy})/\bar{n}\bar{T}$ . These two quantities reach stationary values  $-\bar{P}_{xy,s}/\bar{n}\bar{T}_s \simeq 0.33$  and

$$(\bar{P}_{xx,s} - \bar{P}_{yy,s})/\bar{n}\bar{T}_s \simeq 0.24 \text{ after } s \simeq 40 \text{ (} t/\tau^0 \simeq 8.3\text{)}.$$

In the above comments on Figs. 2–4 we have focused on the physical features of the transient toward the steady-state USF, without distinguishing between the IHS and EHS systems. In fact, as Figs. 2–4 show, the results concerning the hydrodynamic quantities and their fluxes are practically identical in both systems, even when high gradients are transiently present. Therefore, the transport properties of a gas of IHS can be satisfactorily mimicked by a gas of EHS having an adequate diameter and subject to an adequate friction force. However, although a coefficient of restitution  $\alpha = 0.9$  is rather realistic, it is reasonable to expect that this approximate equivalence IHS $\leftrightarrow$ EHS deteriorates as dissipation increases. To analyze this expectation we have considered other values of

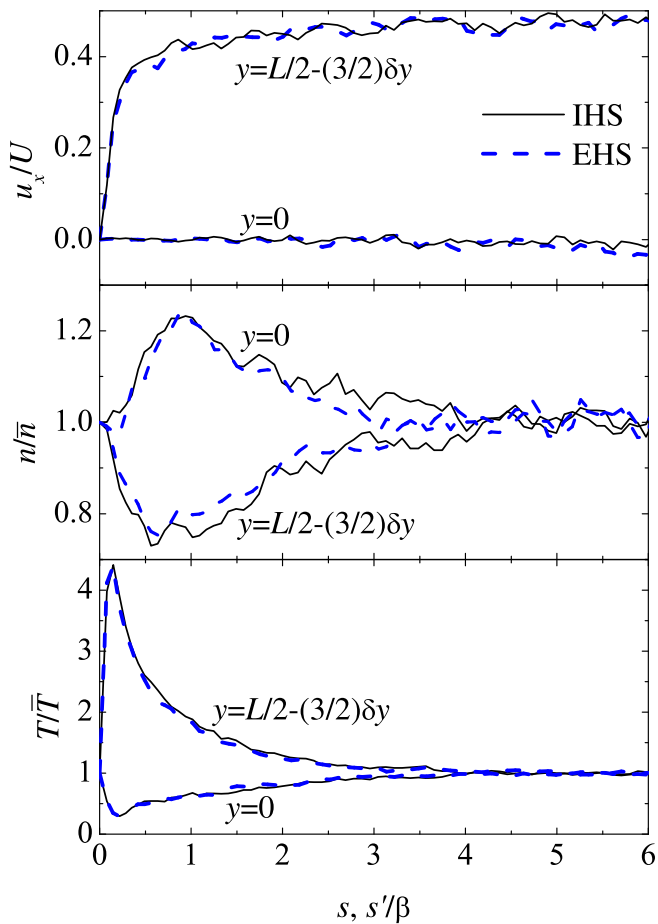


FIG. 3: (Color online) Evolution of the flow velocity, the density, and the temperature around  $y = 0$  and  $y = L/2 - (3/2)\delta y$  for IHS (solid lines) and EHS (dashed lines) in the case  $\alpha = 0.9$ ,  $a\tau^0 = 4$ . Time is measured by the accumulated number of collisions per particle ( $s$ ) in the case of IHS and by the same quantity, but divided by  $\beta$ , ( $s'/\beta$ ) in the case of EHS. The data have been obtained starting from the initial distribution function (3.5).

$\alpha$  in the homogeneous transient problem and, especially, in the steady-state properties.

### B. Homogeneous transient problem

As discussed in Sec. III, the Boltzmann equation for USF allows for solutions which are spatially uniform when the velocities are referred to the (local) Lagrangian frame of reference [cf. Eq. (3.2)]. The simulation of the corresponding Boltzmann equation by the DSMC method is much simpler than in the inhomogeneous problem, as described in Sec. IV B. In these homogeneous simulations we have considered  $\alpha = 0.5$ – $0.95$  (with a step  $\Delta\alpha = 0.05$ ) and two values of the shear rate, namely  $a\tau^0 = 4$  and  $a\tau^0 = 0.1$ . The former value is large enough to make viscous heating initially dominate over (inelastic or frictional) cooling, even for  $\alpha = 0.5$ , so that  $T(t) > T^0$ .

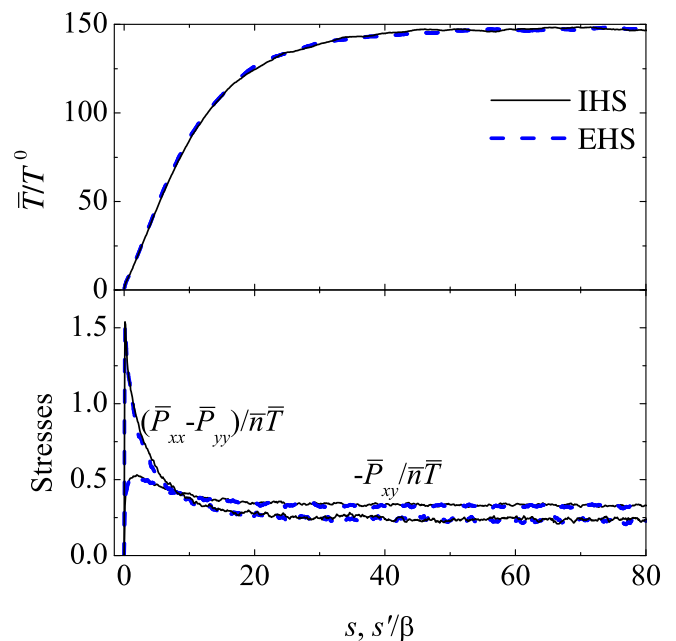


FIG. 4: (Color online) Evolution of  $\bar{T}/T^0$  (top panel) and  $-\bar{P}_{xy}/\bar{n}\bar{T}$  and  $(\bar{P}_{xx} - \bar{P}_{yy})/\bar{n}\bar{T}$  (bottom panel) for IHS (solid lines) and EHS (dashed lines) in the case  $\alpha = 0.9$ ,  $a\tau^0 = 4$ . Time is measured by the accumulated number of collisions per particle ( $s$ ) in the case of IHS and by the same quantity, but divided by  $\beta$ , ( $s'/\beta$ ) in the case of EHS. The data have been obtained starting from the initial distribution function (3.5).

Conversely,  $a\tau^0 = 0.1$  is small enough to produce the opposite effect,  $T(t) < T^0$ , even for  $\alpha = 0.95$ . On the other hand, at a given value of  $\alpha$ , the intrinsic steady-state properties must be independent of the value of the shear rate, and this will provide an important indicator to determine whether the steady state has been reached or not.

Although we have performed simulations for the ten values  $\alpha = 0.5$ – $0.95$ , in this Subsection we will focus on two values:  $\alpha = 0.9$  (moderately small dissipation) and  $\alpha = 0.5$  (large dissipation). In addition to the simulation data for IHS and EHS, we will present the results from the solution of an extension [4, 7] of the Bhatnagar–Gross–Krook (BGK) model [50], which is inspired in the approximate equivalence IHS $\leftrightarrow$ EHS. The solution of this BGK-like model for the USF problem is worked out in Refs. [4, 6, 26].

We begin by showing the accumulated number of collisions per particle as a function of time in Fig. 5, where the case  $\alpha = 0.7$  is also included. As said in connection with Fig. 1, the slope of  $s(t)$  and  $s'(t)$  is proportional to  $\sqrt{T(t)}$ . At a shear rate  $a\tau^0 = 4$ , viscous heating dominates and so the temperature monotonically increases, especially for  $\alpha = 0.9$ ; on the other hand, at  $a\tau^0 = 0.1$ , dissipative cooling prevails and so the temperature monotonically decreases, especially for  $\alpha = 0.5$ . The almost perfect agreement between  $s(t)$  and  $s'(t)/\beta$  for  $\alpha = 0.9$

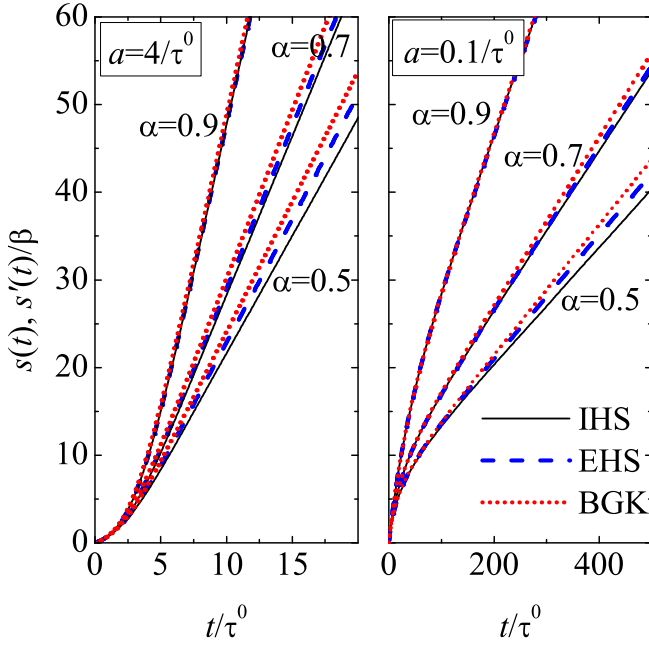


FIG. 5: (Color online) Accumulated number of collisions per particle as a function of time for IHS [ $s(t)$ , solid lines] and for EHS [ $s'(t)$ , dashed lines], in the latter case divided by  $\beta = \frac{1}{2}(1 + \alpha)$ , in the cases  $\alpha = 0.5, 0.7$ , and  $0.9$ . The left panel corresponds to a shear rate  $a\tau^0 = 4$ , while the right panel corresponds to  $a\tau^0 = 0.1$ . The dotted lines are the predictions obtained from the solution of a BGK model. Note that in the right panel the curves corresponding to IHS, EHS, and BGK at  $\alpha = 0.9$  are practically indistinguishable. The data have been obtained starting from the initial distribution function (3.12).

is an indirect indication that  $T(t)$  is practically the same for the IHS gas and the EHS gas, as will be confirmed later on. However, as the inelasticity increases, so does the temperature difference in both systems, the EHS system having a slightly higher temperature than the IHS system at any given time  $t$ . Despite its simplicity, the BGK model does quite good a job, but it tends to overestimate both  $s(t)$  and  $s'(t)/\beta$ . It must be said that the BGK curves for  $s(t)$  have actually been obtained from the local equilibrium approximation (3.13). As we will see, the BGK temperature presents a very good agreement with the simulation results for EHS, so that the small discrepancies between the DSMC curves for  $s'(t)/\beta$  and the BGK curves are essentially due to the local equilibrium approximation  $s(t) \rightarrow s_0(t)$  used in the latter.

To confirm this point, we plot in Fig. 6 the ratio between the actual number of accumulated collisions per particle and the local equilibrium estimate obtained from Eq. (3.13) by a numerical integration using the actual values of temperature. Except for a short initial period,  $s(t)/s_0(t)$  and  $s'(t)/s'_0(t)$  take values smaller than 1 and tend to steady-state values practically independent of the shear rate. The instantaneous collision rate is proportional to the average value of the relative speed

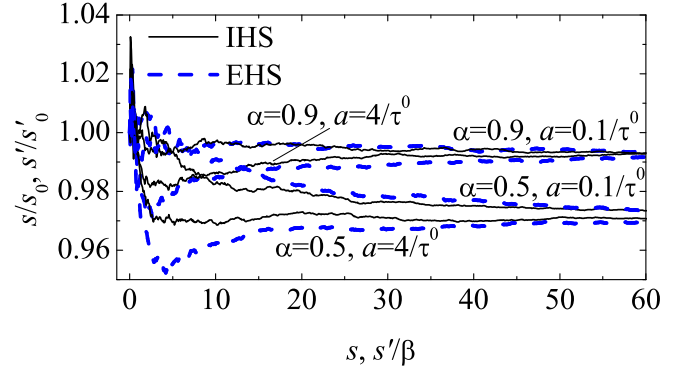


FIG. 6: (Color online) Evolution of the ratio between the actual number of collisions per particle and the local equilibrium estimate for IHS (solid lines) and EHS (dashed lines) in the cases  $\alpha = 0.5, 0.9$  and  $a\tau^0 = 0.1, 4$ . The data have been obtained starting from the initial distribution function (3.12).

$\langle V_{12} \rangle$ , which in the local equilibrium approximation is  $\langle V_{12} \rangle \rightarrow \langle V_{12} \rangle_0 = \sqrt{2} \langle V \rangle_0 = 4\sqrt{T/\pi m}$ . Thus, the fact that  $s(t) < s_0(t)$  is consistent with a nonequilibrium velocity distribution such that the mean speed is smaller than the local equilibrium one, i.e.,  $\langle V \rangle < \langle V \rangle_0$ , this effect being more noticeable as the dissipation increases. By definition,  $\langle V^2 \rangle = \langle V^2 \rangle_0 = 3T/m$ . Therefore, the inequality  $\langle V \rangle < \langle V \rangle_0$  indicates an underpopulation of the region of moderately low velocities of the nonequilibrium distribution function (with respect to the Maxwellian) that compensates for an overpopulation of the high-velocity region, as will be seen later.

The evolution of the relative temperature  $T/T^0$ , the reduced shear stress  $-P_{xy}/nT$ , and the reduced normal stress difference  $(P_{xx} - P_{yy})/nT$  is displayed in Figs. 7 and 8 for  $\alpha = 0.9$  and  $\alpha = 0.5$ , respectively. In the former case, an excellent agreement between the simulation results for both types of system exists. In addition, the theoretical results obtained from the BGK model accurately describe the behavior of the simulation data. In the case  $\alpha = 0.5$ , however, the EHS system tends to have a larger temperature than the IHS system, the steady-state value being about 12% larger in the former case than in the latter. This is partially due to the fact that the true cooling rate  $\zeta$  of the IHS gas [cf. Eq. (2.10)] is larger than the local equilibrium value  $\zeta_0$  [cf. Eq. (2.16)] imposed on the EHS gas, as we will see later on. This also explains why the BGK model, which also makes use of the approximation  $\zeta \rightarrow \zeta_0$ , predicts a temperature in good agreement with the simulation data for EHS. Since the EHS temperature is larger than the IHS one, the shear rate normalized with the collision rate is smaller for EHS than for IHS and, consequently, the distortion with respect to the Maxwellian, as measured by the shear stress and, especially, by the normal stress difference, is smaller in the former case than in the latter. Comparison between Figs. 7 and 8 shows that the duration of the transient period (as measured by the number of col-

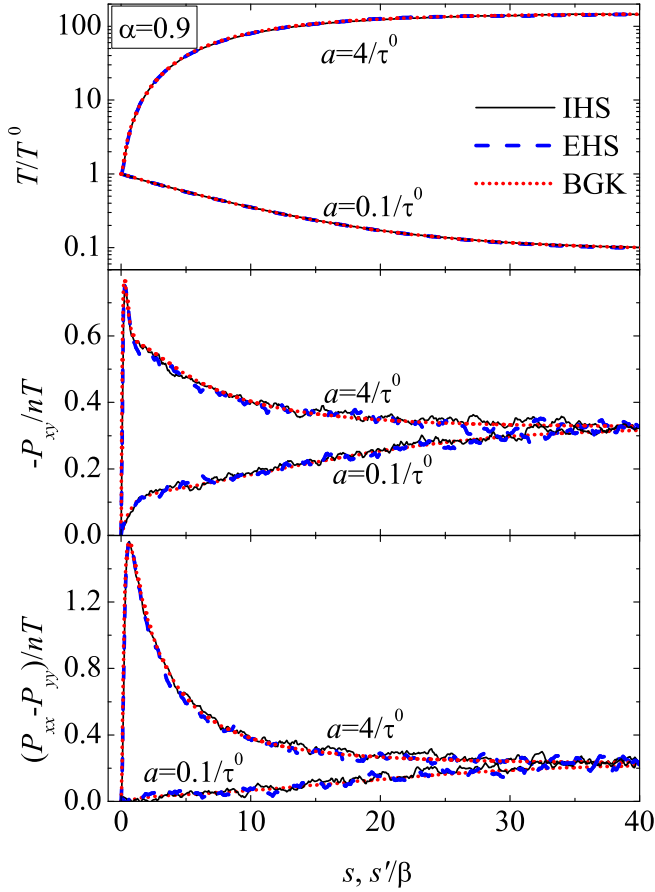


FIG. 7: (Color online) Evolution of  $T/T^0$ ,  $-P_{xy}/nT$ , and  $(P_{xx} - P_{yy})/nT$  for IHS (solid lines) and EHS (dashed lines) in the cases  $\alpha = 0.9$  with  $a\tau^0 = 0.1$  and  $a\tau^0 = 4$ . The dotted lines are the predictions obtained from the solution of a BGK model. Note that in the top panel the curves corresponding to IHS, EHS, and BGK are practically indistinguishable. The data have been obtained starting from the initial distribution function (3.12).

lisions per particle) decreases as the inelasticity increases:  $s \simeq 40$  at  $\alpha = 0.9$  versus  $s \simeq 20$  at  $\alpha = 0.5$ . However, when that duration is measured in real units, it depends mainly on the shear rate and not on  $\alpha$ , namely  $t \simeq 9\tau^0$  for  $a\tau^0 = 4$  and  $t \simeq 160-200\tau^0$  for  $a\tau^0 = 0.1$ .

It is interesting to note the similarity between the curves in Fig. 4 and those corresponding to  $a\tau^0 = 4$  in Fig. 7. This is made clear in Fig. 9, where the evolution of the global quantities in the IHS case for the homogeneous and inhomogeneous transient problems are shown. In the three situations considered, the initial shear stress and normal stress differences are zero; however, given the high value of the shear rate, the velocity distribution function rapidly changes and adapts itself to the imposed shear rate, giving rise to a sharp maximum of the reduced shear stress and normal stress difference. Henceforth, as the temperature increases so does the collision rate, so that the *relative* strength of the shear rate becomes smaller and smaller until the steady state is reached at

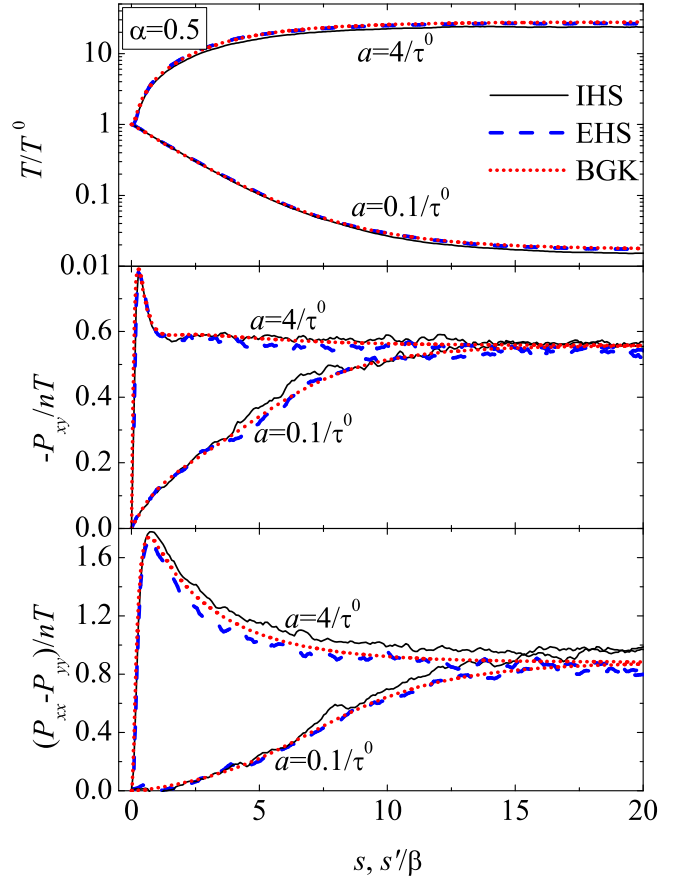


FIG. 8: (Color online) Evolution of  $T/T^0$ ,  $-P_{xy}/nT$ , and  $(P_{xx} - P_{yy})/nT$  for IHS (solid lines) and EHS (dashed lines) in the cases  $\alpha = 0.5$  with  $a\tau^0 = 0.1$  and  $a\tau^0 = 4$ . The dotted lines are the predictions obtained from the solution of a BGK model. The data have been obtained starting from the initial distribution function (3.12).

$s \approx 40$ . The first stage lasts about one collision per particle, has a kinetic nature, and is sensitive to the initial preparation of the system. On the other hand, the subsequent relaxation toward the steady state defines a much longer *hydrodynamic* stage that becomes more and more independent of the initial state, provided that  $T^0 < T_s$ . A similar hydrodynamic regime exists for the class of initial states with  $T^0 > T_s$  (e.g., for  $a\tau^0 = 0.1$ ). These comments also apply to the two cases with  $\alpha = 0.5$ .

In general, at a given value of  $\alpha$ , the *intrinsic* velocity distribution function in the hydrodynamic regime depends on time only through its dependence on the shear rate nondimensionalized with the (time-dependent) collision rate. More specifically,

$$f(\mathbf{V}, t) = n \left[ \frac{m}{2T(t)} \right]^{3/2} f^*(\mathbf{C}(t); a^*(t)), \quad (5.1)$$

where

$$\mathbf{C}(t) = \frac{\mathbf{V}}{\sqrt{2T(t)/m}}, \quad a^*(t) = a\tau_\eta(t). \quad (5.2)$$

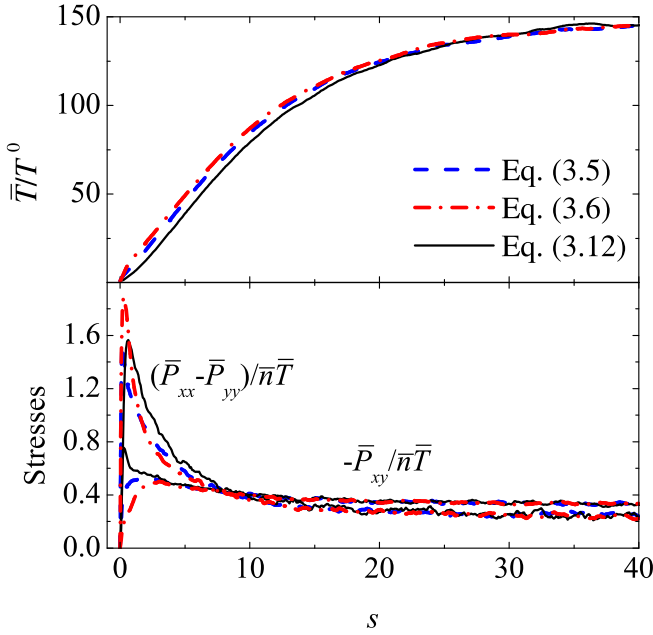


FIG. 9: (Color online) Evolution of  $\bar{T}/T^0$  (top panel) and  $-\bar{P}_{xy}/\bar{n}\bar{T}$  and  $(\bar{P}_{xx} - \bar{P}_{yy})/\bar{n}\bar{T}$  (bottom panel) for IHS in the case  $\alpha = 0.9$ ,  $a\tau^0 = 4$ . The dashed and dash-dot lines correspond to the inhomogeneous transient problem with the initial conditions (3.5) and (3.6), respectively, while the solid lines correspond to the homogeneous transient problem with the initial conditions (3.12).

The definition of the reduced shear rate  $a^*$  by means of the viscosity characteristic time  $\tau_\eta$  instead of the mean free time  $\tau_{\text{mft}}$  or the characteristic time  $\tau$  is an irrelevant matter of choice since these three quantities differ only by constant factors, namely  $\tau_{\text{mft}}/\tau_\eta \simeq 0.787$  and  $\tau/\tau_\eta \simeq 0.888$ . In the steady state,  $a^*(t) \rightarrow a_s^*$  and  $f^*(\mathbf{C}; a^*) \rightarrow f^*(\mathbf{C}; a_s^*) = f_s^*(\mathbf{C})$  [cf. Eq. 3.16].

During the hydrodynamic relaxation toward the steady state, it is insightful to define a time-dependent shear viscosity  $\eta(t) = -P_{xy}(t)/a$ . As a consequence of Eq. (5.1), the ratio  $\eta(t)/\eta_0(t)$ , where  $\eta_0(t) = nT(t)\tau_\eta(t)$  is the Navier–Stokes viscosity in the elastic limit [cf. Eq. (2.18)], depends on time only through a nonlinear dependence on  $a^*(t)$ . Figure 10 shows the reduced shear viscosity  $\eta^* \equiv \eta/\eta_0$  versus the reduced shear rate  $a^*$  in the case  $\alpha = 0.5$ . The values plotted correspond to a temporal window  $2 \lesssim s \lesssim 50$ . The lower limit guarantees that the system has practically lost memory of its initial state, while the upper limit is long enough to guarantee that the steady state (represented by an open symbol) has been reached. For each case (IHS, EHS, or BGK), the steady-state point  $(a_s^*, \eta_s^*)$  splits the respective curve into two branches: the one to the left of the point corresponds to  $T < T^0$  (e.g.,  $a\tau^0 = 0.1$ ), while the branch to the right corresponds to  $T > T^0$  (e.g.,  $a\tau^0 = 4$ ). The entire curve represents the *nonlinear* shear viscosity  $\eta^*(a^*)$  for  $\alpha = 0.5$ , and the steady-state point  $\eta_s^* = \eta^*(a_s^*)$  is just a particular (and singular) value [6]. The formal extrap-

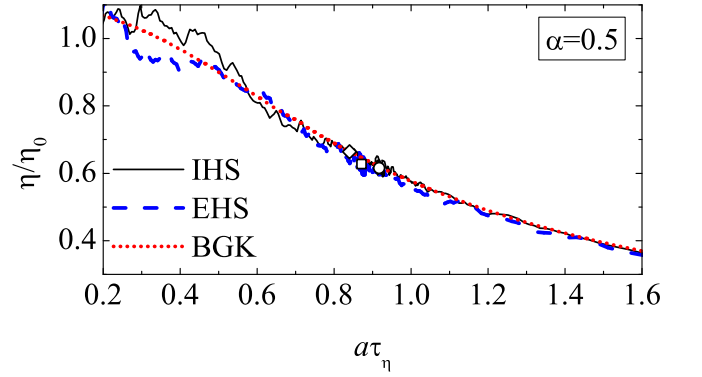


FIG. 10: (Color online) (Transient) reduced shear viscosity  $\eta^*(t) \equiv \eta(t)/\eta_0(t)$  versus the (transient) reduced shear rate  $a^*(t) \equiv a\tau_\eta(t)$  for IHS (solid lines) and EHS (dashed lines) in the case  $\alpha = 0.5$ . The dotted lines are the predictions obtained from the solution of a BGK model. The circle, square, and diamond are the steady-state points for IHS, EHS, and BGK, respectively. In each case, the curve to the left of the symbol corresponds to  $a\tau^0 = 0.1$ , while the curve to the right of the symbol corresponds to  $a\tau^0 = 4$ .

olation of  $\eta^*(a^*)$  to zero shear rate gives the (reduced) Navier–Stokes shear viscosity  $\eta_{\text{NS}}^* = \lim_{a^* \rightarrow 0} \eta^*(a^*)$  at  $\alpha = 0.5$ . The expected values are [4, 8]  $\eta_{\text{NS}}^* \simeq 1.3$  for IHS and  $\eta_{\text{NS}}^* \simeq 1.1$  for EHS and BGK. It is worthwhile noting that, except for fluctuations in the simulation data, the curves  $\eta^*(a^*)$  for IHS, EHS, and BGK practically coincide, at least in the interval  $0.2 < a^* < 1.6$ . Thus, the main difference among the three approaches lies in the steady-state point where the system “decides” to stop. For a more extensive discussion on the rheological function  $\eta^*(a^*)$  and the distinction between  $\eta_s^*$  and  $\eta_{\text{NS}}^*$  the reader is referred to Ref. [6].

Although the most relevant information in the USF problem is conveyed by the elements of the pressure tensor, they of course do not exhaust the physical information one can extract from the simulations. In Figs. 11 and 12 we present the evolution of the ratio  $\langle V_{12}^3 \rangle / \langle V_{12}^3 \rangle_0$  (where  $V_{12}$  is the relative speed between a pair of particles) and the fourth and sixth cumulants [cf. Eq. (3.14)] for  $\alpha = 0.9$  and  $\alpha = 0.5$ , respectively. The average value  $\langle V_{12}^3 \rangle$  is physically interesting because it is proportional to the true cooling rate  $\zeta$  of the IHS gas. In fact, we have checked in the simulations that the value of  $\zeta$  obtained from Eq. (2.10) agrees with the one computed directly from the collisional energy loss, Eq. (2.9). However, the second method is much noisier than the first one since it involves only the colliding pairs, whereas all the pairs contribute to  $\langle V_{12}^3 \rangle$  [see, however, Eq. (4.20) and the comment above it].

As happened with Figs. 7 and 8, the simulation data for each one of the three plotted quantities in the case  $a\tau^0 = 4$  present a respective maximum during the kinetic stage of the evolution, representing the largest departure from the Maxwellian. It is noteworthy that the fluctuations of the quantities plotted in Figs. 11 and 12 are much larger

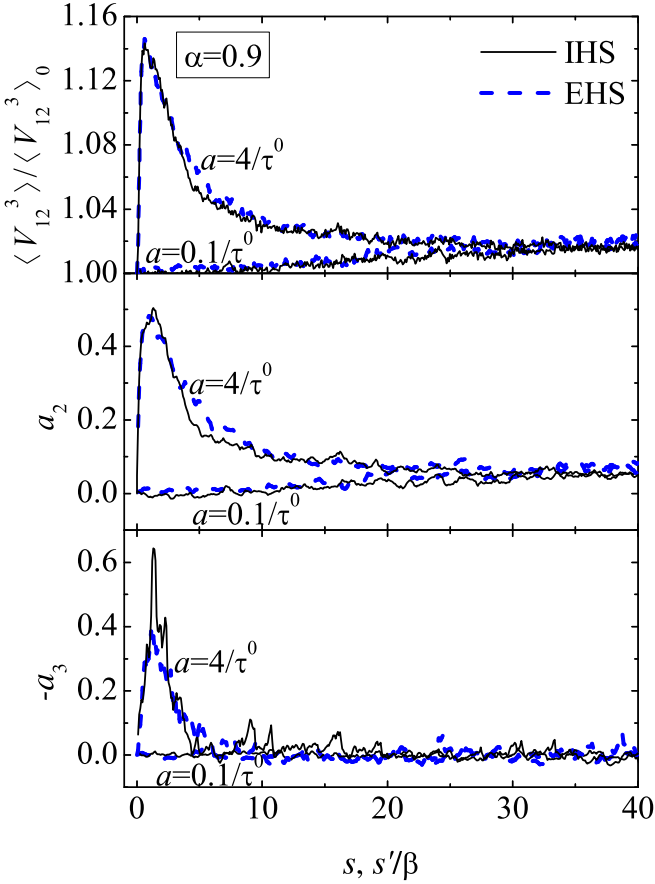


FIG. 11: (Color online) Evolution of the ratio  $\langle V_{12}^3 \rangle / \langle V_{12}^3 \rangle_0$ , the fourth cumulant  $a_2$ , and the sixth cumulant  $-a_3$  for IHS (solid lines) and EHS (dashed lines) in the cases  $\alpha = 0.9$  with  $a\tau^0 = 0.1$  and  $a\tau^0 = 4$ . The data have been obtained starting from the initial distribution function (3.12).

in the IHS case than in the EHS case. Otherwise, the temporal evolution and the steady-state values are very similar in both systems.

We observe that  $\langle V_{12}^3 \rangle > \langle V_{12}^3 \rangle_0$ , the relative difference increasing with the inelasticity. This explains that the (internal) collisional cooling rate  $\zeta$  of the IHS gas is larger than the (external) frictional cooling rate  $\zeta_0$  imposed on the EHS gas, as said before in connection with Fig. 8. However, even though the imposed cooling rate for EHS is the local equilibrium one, this system satisfactorily mimics the distortion from local equilibrium, as measured by  $\langle V_{12}^3 \rangle / \langle V_{12}^3 \rangle_0$ , of the IHS system.

The cumulants basically probe the high-energy tail of the distribution, especially in the case of  $a_3$ . The positive value of the fourth cumulant  $a_2$ , both for IHS and EHS, is a reflection of a strong high-energy overpopulation (with respect to the Maxwellian) induced by the shearing. This overpopulation effect is larger than and essentially independent of the one typically present in homogeneous states of granular gases [51, 52], which is absent in the EHS gas. The steady-state value of the

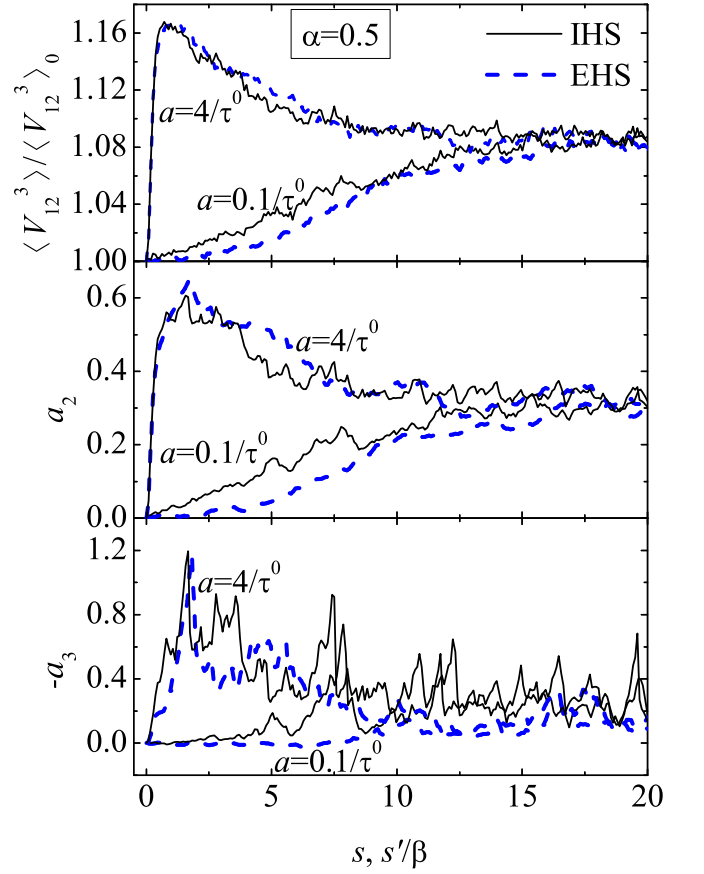


FIG. 12: (Color online) Evolution of the ratio  $\langle V_{12}^3 \rangle / \langle V_{12}^3 \rangle_0$ , the fourth cumulant  $a_2$ , and the sixth cumulant  $-a_3$  for IHS (solid lines) and EHS (dashed lines) in the cases  $\alpha = 0.5$  with  $a\tau^0 = 0.1$  and  $a\tau^0 = 4$ . The data have been obtained starting from the initial distribution function (3.12).

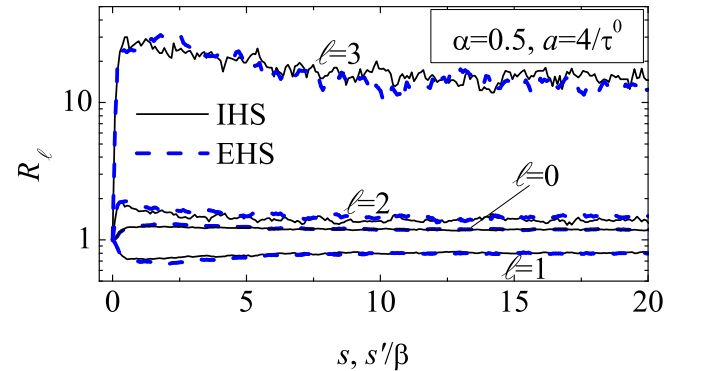


FIG. 13: (Color online) Evolution of the ratios  $R_0, R_1, R_2$ , and  $R_3$  [cf. Eq. (3.15)] for IHS (solid lines) and EHS (dashed lines) in the case  $\alpha = 0.5$  with  $a\tau^0 = 4$ . The data have been obtained starting from the initial distribution function (3.12).

sixth cumulant  $a_3$  is practically zero for  $\alpha = 0.9$ . On the other hand, for  $\alpha = 0.5$  one has  $-a_3 > 0$ , what is again related to the high-energy overpopulation.

A more direct information about the evolution of the velocity distribution is provided by the ratios  $R_\ell$  defined by Eq. (3.15). They are plotted in Fig. 13 for the case  $\alpha = 0.5$  and  $a\tau^0 = 4$ . The maximum deviation from the Maxwellian takes place during the kinetic stage ( $s \lesssim 1$ ). Thereafter, the curves smoothly relax toward their steady-state values  $R_0 \simeq 1.18$ ,  $R_1 \simeq 0.81$ ,  $R_2 \simeq 1.39$ , and  $R_3 \simeq 15$ , the relaxation times being practically the same ( $s \approx 10$ ) in the four cases. During the hydrodynamic transient regime and in the steady state, the population of particles moving with a speed larger than three times the thermal speed  $v_0(t) = \sqrt{2T(t)/m}$  is remarkably larger than the one expected from a Maxwellian distribution. This overpopulation effect induced by shearing is also present in the interval  $2v_0(t) < V < 3v_0(t)$ . In the hydrodynamic transient regime, between 90% and 93% of the particles move with a speed smaller than  $2v_0(t)$  (in contrast to the equilibrium value of 95.4%) and this is then the relevant region for the low-degree moments. While the low-velocity region  $V < v_0(t)$  is about 20% overpopulated with respect to the Maxwellian, the intermediate region  $v_0(t) < V < 2v_0(t)$  is underpopulated by about the same amount. In fact, the fraction of particles moving with  $V < v_0(t)$  and  $v_0(t) < V < 2v_0(t)$  is about 51% and 42%, respectively, in the steady state, while the corresponding equilibrium values are 42.8% and 52.6%, respectively. As Fig. 13 shows, all these features are successfully captured by the EHS system, even at this rather high inelasticity.

The fact that  $\langle V_{12}^3 \rangle > \langle V_{12}^3 \rangle_0$  suggests that a better agreement between the dynamics of the IHS gas and that of the EHS gas could be expected if the friction constant of the latter were not chosen as  $\gamma = \frac{1}{2}\zeta_0$  but as  $\gamma = \frac{1}{2}\zeta_0 \langle V_{12}^3 \rangle / \langle V_{12}^3 \rangle_0$ , so that the cooling rate of the EHS gas would be exactly the same functional of  $f$  as that of the IHS gas. To test this expectation, we have carried out supplementary simulations of the EHS system with this more refined friction constant in the case  $\alpha = 0.5$ ,  $a\tau^0 = 4$ . The corresponding curves are not included in Figs. 5, 6, 8, 10, 12, and 13 for the sake of clarity. The results show that, in general, the quantities associated with the low-order moments (temperature and pressure tensor) are indeed closer to the IHS values than with the simpler choice  $\gamma = \frac{1}{2}\zeta_0$ . As a matter of fact, the EHS temperature is now slightly smaller, instead of slightly larger, than the IHS temperature. However, in the cases of  $\langle V_{12}^3 \rangle / \langle V_{12}^3 \rangle_0$ ,  $a_2$ , and  $a_3$ , the results obtained in the EHS simulations with  $\gamma = \frac{1}{2}\zeta_0 \langle V_{12}^3 \rangle / \langle V_{12}^3 \rangle_0$  turn out to be not necessarily better than those obtained with  $\gamma = \frac{1}{2}\zeta_0$ .

### C. Steady state

Once we have analyzed the transient period toward the steady state for the representative cases  $\alpha = 0.5$  and  $\alpha =$

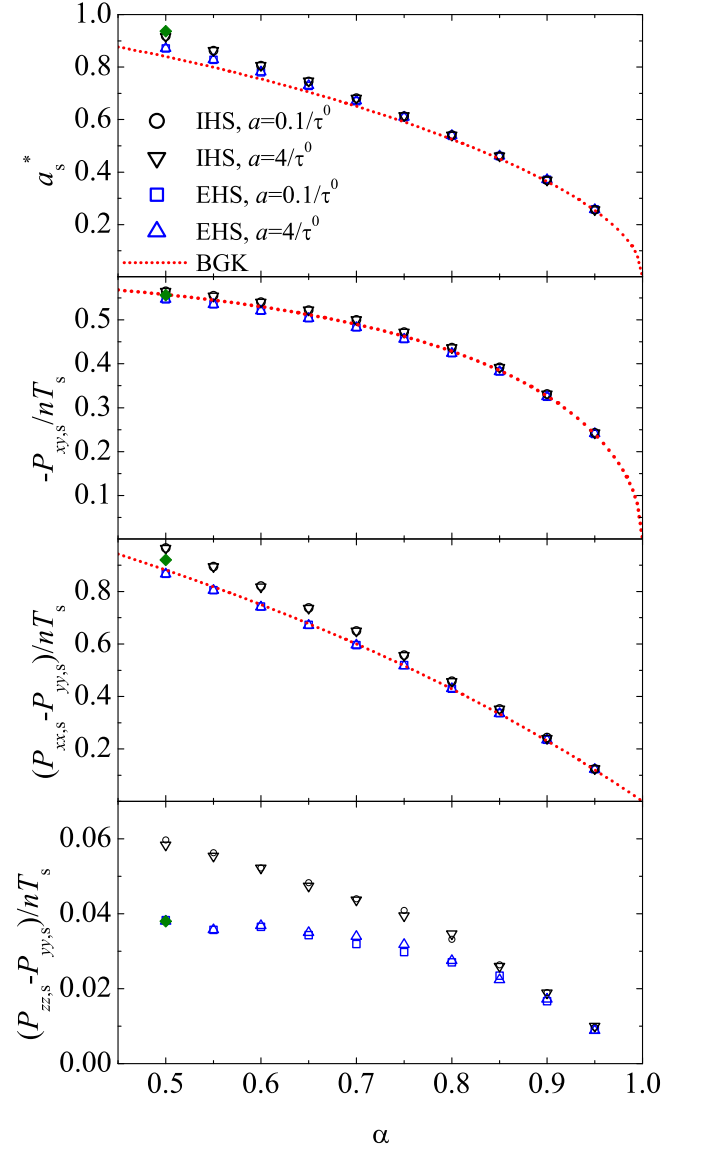


FIG. 14: (Color online) Steady-state values of the reduced shear rate  $a^* = a\tau_\eta$ , the reduced shear stress  $-P_{xy}/nT$ , and the reduced normal stress differences  $(P_{xx} - P_{yy})/nT$  and  $(P_{zz} - P_{yy})/nT$  as functions of the coefficient of restitution  $\alpha$ . The open symbols are simulation results for IHS and EHS and two values of the shear rate, while the dotted lines correspond to the solution of a BGK model. Note that in the latter model  $P_{zz,s} = P_{yy,s}$ . The filled diamonds represent simulation data of EHS with a friction constant  $\gamma = \frac{1}{2}\zeta_0 \langle V_{12}^3 \rangle / \langle V_{12}^3 \rangle_0$  in the case  $\alpha = 0.5$ ,  $a\tau^0 = 4$ .

0.9, let us report on the most relevant steady-state properties for all the values  $\alpha = 0.5-0.95$  we have considered. The quantities associated with the second-degree velocity moments, namely the reduced shear rate  $a_s^* = a\tau_\eta(T_s) \propto 1/\sqrt{T_s}$ , the reduced shear stress  $-P_{xy,s}/nT_s$ , and the reduced normal stress differences  $(P_{xx,s} - P_{yy,s})/nT_s$  and  $(P_{zz,s} - P_{yy,s})/nT_s$ , are plotted in Fig. 14. The overlapping of the data obtained from simulations with the

two different values of the shear rate ( $a\tau^0 = 0.1$  and  $a\tau^0 = 4$ ) confirms that the steady state has actually been reached and that the intrinsic velocity distribution function  $f_s^*(\mathbf{C})$  [cf. Eq. (3.16)] depends only on  $\alpha$  and not on the initial preparation of the system. For  $\alpha \gtrsim 0.7$  there exists a good agreement between the EHS and IHS results for the quantities  $a_s^*$  and  $-P_{xy,s}/nT_s$ , which are the most relevant properties in the USF problem. For larger inelasticity, however, the steady-state temperature  $T_s$  is larger for the EHS gas than for the IHS gas, and so  $a_s^*$  is smaller in the former case than in the latter. This implies that the departure from isotropy is slightly smaller in the EHS gas than in the IHS gas, and so is the shear stress  $-P_{xy,s}/nT_s$ . As for the normal stress differences ( $P_{xx,s} - P_{yy,s})/nT_s$  and, especially,  $(P_{zz,s} - P_{yy,s})/nT_s$ , they start to differ in both systems for  $\alpha \lesssim 0.85$ . It is worthwhile noting that the BGK kinetic model, which has a simple explicit solution in the steady state [4, 6], does a very good job at predicting the transport properties, especially in the case of the EHS system. An exception is the normal stress difference  $(P_{zz,s} - P_{yy,s})/nT_s$ , which vanishes in the BGK model but takes on (small) positive values in the simulations. The good agreement between simulation data for the elements of the pressure tensor and the BGK predictions was already noted in Ref. [26], although there the kinetic model was slightly different from the one considered here.

Figure 14 also includes results obtained from control simulations carried out in the case  $\alpha = 0.5$  on EHS but with a refined friction constant  $\gamma = \frac{1}{2}\zeta_0\langle V_{12}^3\rangle/\langle V_{12}^3\rangle_0$  instead of the simple one  $\gamma = \frac{1}{2}\zeta_0$ . We observe that the agreement with the IHS data improves for those quantities that were already reasonably well described by the simple EHS system, namely  $T_s$ ,  $P_{xy,s}$ , and  $P_{xx,s} - P_{yy,s}$ . On the other hand, the delicate normal stress difference  $P_{zz,s} - P_{yy,s}$ , which otherwise is quite small, is still about 40% smaller in both EHS systems than in the IHS system. This indicates that whenever the discrepancies between the IHS and EHS results are relatively important, they are hardly affected by a more sophisticated choice of the friction constant  $\gamma$ .

From a rheological point of view, it is worthwhile introducing the nonlinear shear viscosity  $\eta^* = -(P_{xy}/a)/\eta_0 = -(P_{xy}/nT)/a^*$  and the viscometric functions  $\Psi_1 = (P_{yy} - P_{xx})/nTa^{*2}$  and  $\Psi_2 = (P_{zz} - P_{yy})/nTa^{*2}$ . In the hydrodynamic transient regime, they are functions of  $a^*$  (for a given value of  $\alpha$ ), as was illustrated in Fig. 10 in the case of  $\eta^*$  at  $\alpha = 0.5$ . In the steady state ( $a^* \rightarrow a_s^*$ ) these quantities become functions of  $\alpha$  only. Equivalently, by eliminating  $\alpha$  in favor of the steady-state reduced shear rate  $a_s^*$ , those rheological quantities can be seen as functions of  $a_s^*$ . This is the representation shown in Fig. 15. We observe that the curve  $\eta_s^*(a_s^*)$  for EHS is very close to the one for IHS, even though the EHS points are shifted with respect to the IHS points corresponding to the same value of  $\alpha$ , the shift increasing as  $\alpha$  decreases. On the other hand, the viscometric effects are more pronounced in the IHS case than in the EHS

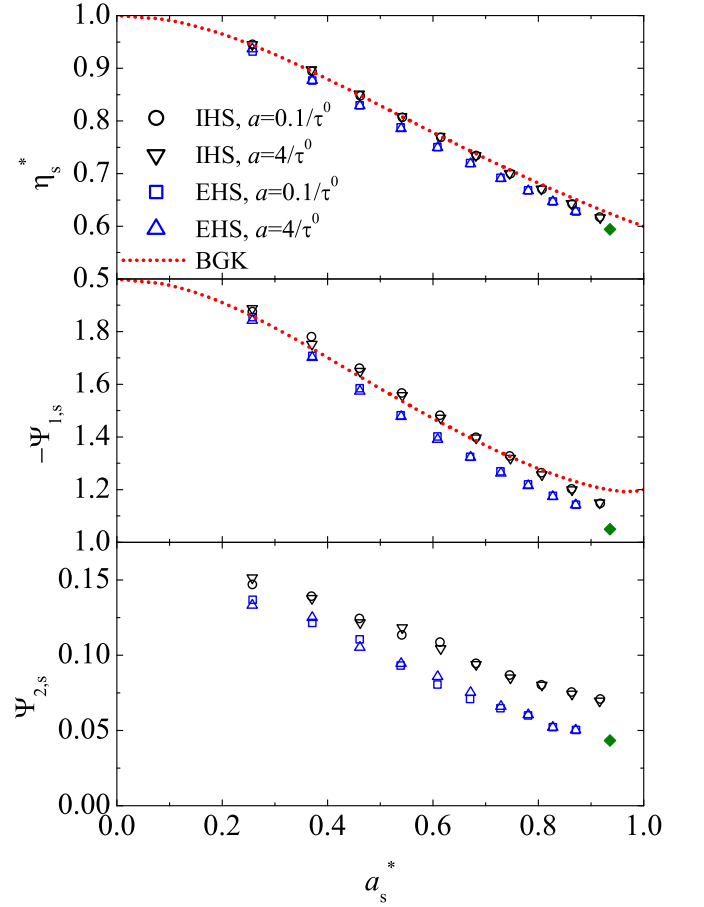


FIG. 15: (Color online) Steady-state values of the reduced shear viscosity  $\eta^* = \eta/\eta_0$  and the viscometric functions  $-\Psi_1 = (P_{xx} - P_{yy})/nTa^{*2}$  and  $\Psi_2 = (P_{zz} - P_{yy})/nTa^{*2}$  as functions of the reduced shear rate  $a_s^*$ . The open symbols are simulation results for IHS and EHS. Two values of the shear rate, while the dotted lines correspond to the solution of a BGK model. Note that in the latter model  $\Psi_{2,s} = 0$ . The filled diamonds represent simulation data of EHS with a friction constant  $\gamma = \frac{1}{2}\zeta_0\langle V_{12}^3\rangle/\langle V_{12}^3\rangle_0$  in the case  $\alpha = 0.5$ ,  $a\tau^0 = 4$ .

case. Paradoxically, the BGK curves for  $\eta_s^*$  and  $\Psi_{1,s}$  are generally closer to IHS than to EHS in the representation of Fig. 15. It is also noteworthy that the isolated points corresponding to EHS with  $\gamma = \frac{1}{2}\zeta_0\langle V_{12}^3\rangle/\langle V_{12}^3\rangle_0$  seems to be consistent with the curve obtained by joining the other EHS points.

The  $\alpha$ -dependence of  $\langle V_{12}^3\rangle/\langle V_{12}^3\rangle_0$  and the cumulants  $a_2$  and  $a_3$  in the steady state is displayed in Fig. 16. We recall that in the IHS system the ratio  $\langle V_{12}^3\rangle/\langle V_{12}^3\rangle_0$  coincides with the ratio  $\zeta/\zeta_0$  between the true cooling rate and its local equilibrium estimate. It is observed that the local equilibrium approximation underestimates the cooling rate by a few percent, essentially due to the distortion induced by the shearing. This distortion is well captured by the EHS system, despite the fact that its cooling rate is, by construction, given by  $\zeta_0$ . As said above, the posi-

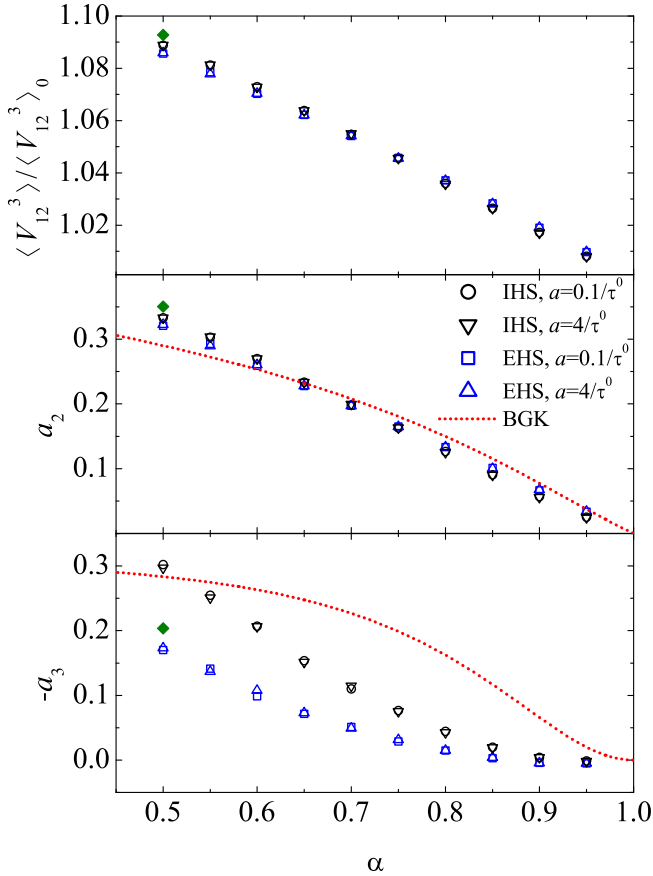


FIG. 16: (Color online) Steady-state values of the the ratio  $\langle V_{12}^3 \rangle / \langle V_{12}^3 \rangle_0$ , the fourth cumulant  $a_2$ , and the sixth cumulant  $-a_3$  as functions of the coefficient of restitution  $\alpha$ . The open symbols are simulation results for IHS and EHS and two values of the shear rate, while the dotted lines in the middle and bottom panels correspond to the solution of a BGK model. The filled diamonds represent simulation data of EHS with a friction constant  $\gamma = \frac{1}{2}\zeta_0 \langle V_{12}^3 \rangle / \langle V_{12}^3 \rangle_0$  in the case  $\alpha = 0.5$ ,  $a\tau^0 = 4$ .

tive values of  $a_2$  and, especially,  $-a_3$  are indicators of an overpopulation effect (with respect to the Maxwellian) of the high-velocity tail of the distribution, this effect being stronger than and practically independent of the typical high-velocity overpopulation of granular gases in uniform and isotropic states [51, 52]. As a matter of fact, the distribution function of the (frictional) EHS gas in the homogeneous cooling state, as well as in the state heated by a white-noise forcing, is exactly a Gaussian. Therefore, the overpopulation measured by  $a_2$  and  $-a_3$  is basically a shearing effect. The fourth cumulant is well accounted for by the EHS gas, but the magnitude of the sixth cumulant is larger for IHS than for EHS. As happens with the normal stress difference  $P_{zz} - P_{yy}$  (see the bottom panel of Fig. 14), the cumulant  $a_3$  is a very sensitive quantity that probes subtle details of the IHS velocity distribution function not sufficiently well captured by the EHS system for  $\alpha \lesssim 0.85$ .

It is worthwhile noting that  $\langle V_{12}^3 \rangle / \langle V_{12}^3 \rangle_0$  and  $a_2$  are slightly larger in the EHS case than in the IHS case for  $\alpha \gtrsim 0.7$ , while the opposite happens for  $\alpha \lesssim 0.7$ . This is reminiscent of the situation in the homogeneous cooling state and in the white-noise heated state [51], where  $a_2^{\text{IHS}} \leq a_2^{\text{EHS}} = 0$  for  $\alpha \geq \sqrt{2}/2 \simeq 0.71$ , while  $a_2^{\text{IHS}} \geq a_2^{\text{EHS}} = 0$  for  $\alpha \leq \sqrt{2}/2$ . In fact, we have observed that the difference  $a_2^{\text{IHS}} - a_2^{\text{EHS}}$  in the USF is quite close to the difference in the white-noise heated state. Figure 16 also shows a strong correlation between the values of  $\langle V_{12}^3 \rangle / \langle V_{12}^3 \rangle_0$  and those of  $a_2$ . More precisely, we have empirically checked that  $\langle V_{12}^3 \rangle / \langle V_{12}^3 \rangle_0 \simeq 1 + 0.27a_2$  both for IHS and EHS in USF, in contrast to  $\langle V_{12}^3 \rangle / \langle V_{12}^3 \rangle_0 \simeq 1 + \frac{3}{16}a_2$  in isotropic states [51].

In Fig. 16 we have included the BGK predictions for the cumulants  $a_2$  and  $a_3$ . Not being associated with conventional velocity moments, the evaluation of  $\langle V_{12}^3 \rangle$  [cf. Eq. (2.11)] from the BGK distribution function requires heavy numerical work and so it is not included in Fig. 16. We observe that the increase of  $a_2$  with increasing inelasticity is well captured by the BGK model. On the other hand, the  $\alpha$ -dependence of  $-a_3$  is described by the BGK model at a qualitative level only, predicting in general too high values.

Regarding the control simulations for EHS with  $\alpha = 0.5$  and  $\gamma = \frac{1}{2}\zeta_0 \langle V_{12}^3 \rangle / \langle V_{12}^3 \rangle_0$ , we observe that the values of  $\langle V_{12}^3 \rangle / \langle V_{12}^3 \rangle_0$  and  $a_2$  are not actually improved, while the improvement on  $a_3$  is very small.

The quantities plotted in Figs. 14–16 provide useful (indirect) information about the velocity distribution function of the steady-state USF. However, they essentially probe the domain of low and moderate velocities (say  $V \lesssim 2\sqrt{2T/m}$ ), except perhaps in the cases of  $a_2$  and, especially,  $a_3$ , which are more sensitive to the high-velocity tail. In order to analyze more directly the shape of the velocity distribution, its anisotropy, and the high-velocity tail, we have measured in the simulations the steady-state marginal distributions defined by Eqs. (3.18)–(3.20). As representative examples, Figs. 17 (linear scale) and 18 (logarithmic scale) show  $g_x^{(+)}(C_x)$ ,  $g_y^{(+)}(C_y)$ , and  $F(C)$  for  $\alpha = 0.9$  and  $\alpha = 0.5$ . We have checked that the symmetry properties (3.21) are fulfilled and that the curves obtained from the two values of the shear rate ( $a\tau^0 = 4$  and  $a\tau^0 = 0.1$ ) practically coincide. In fact, to improve the statistics, the simulation data represented in Fig. 18 have been averaged over both shear rates and, in addition, the symmetry properties (3.21) have been exploited to make

$$\begin{aligned} g_x^{(+)}(C_x) &\rightarrow \frac{1}{2} \left[ g_x^{(+)}(C_x) + g_x^{(-)}(-C_x) \right], \\ g_y^{(+)}(C_y) &\rightarrow \frac{1}{2} \left[ g_y^{(+)}(C_y) + g_y^{(-)}(-C_y) \right]. \end{aligned} \quad (5.3)$$

Two anisotropic features of the USF state are quite apparent. First, the functions  $g_x^{(+)}(C_x)$  and  $g_y^{(+)}(C_y)$  are clearly asymmetric, namely  $g_x^{(+)}(|C_x|) < g_x^{(+)}(-|C_x|)$  and  $g_y^{(+)}(|C_y|) < g_y^{(+)}(-|C_y|)$ . This is a physical effect induced by the shearing, in consistency with  $P_{xy} \propto$

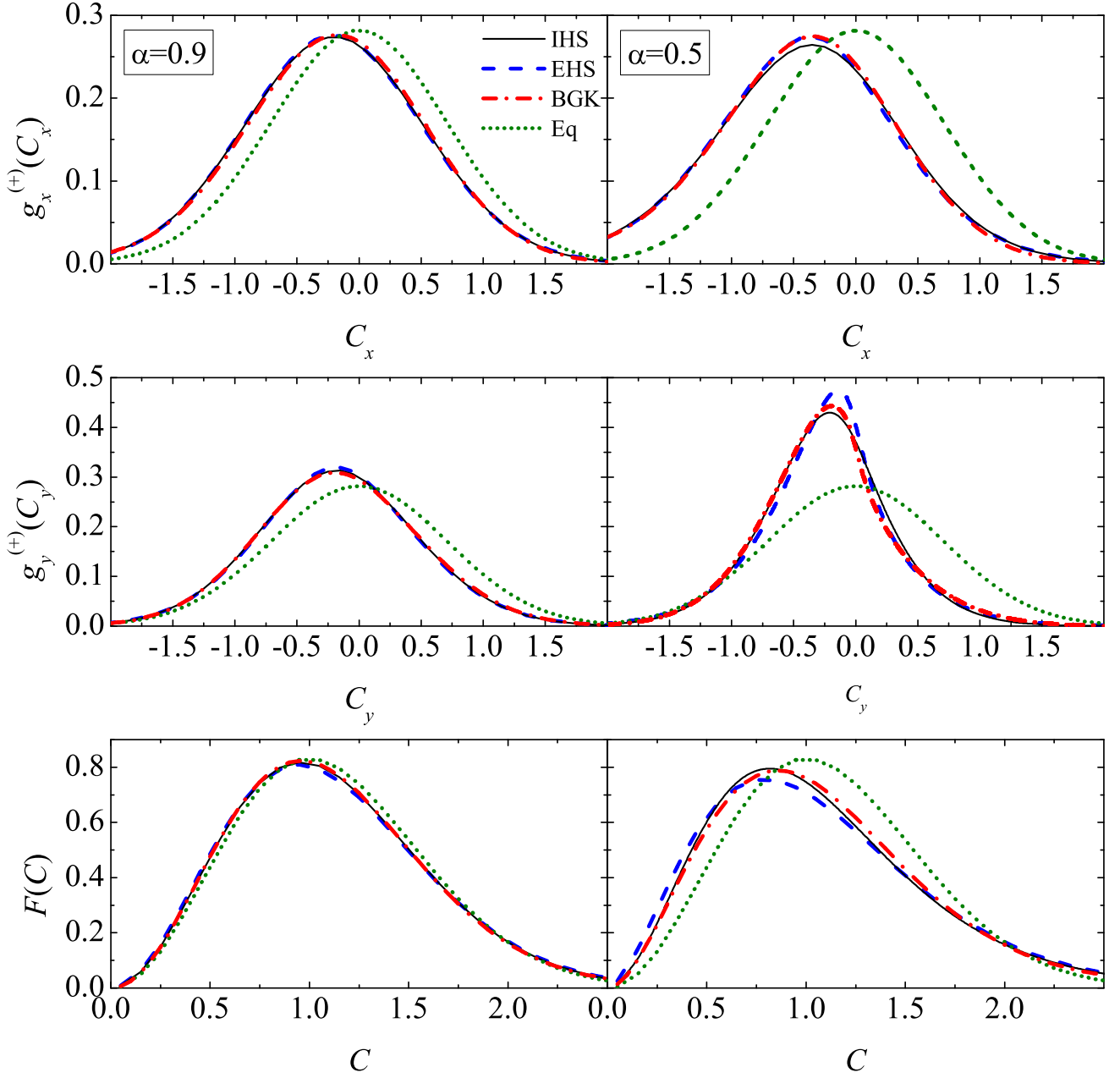


FIG. 17: (Color online) Linear plots of the marginal velocity distribution functions  $g_x^{(+)}(C_x)$ ,  $g_y^{(+)}(C_y)$ , and  $F(C)$  for  $\alpha = 0.9$  (left panels) and  $\alpha = 0.5$  (right panels). The solid and dashed lines represent simulation results for IHS and EHS, respectively, the dash-dot lines are the BGK predictions, and the dotted lines are the (local) equilibrium distributions.

$\langle C_x C_y \rangle < 0$ . The second feature is the non-Newtonian property  $g_x^{(+)} \neq g_y^{(+)}$ . More specifically, the marginal distribution  $g_x^{(+)}$  is broader than  $g_y^{(+)}$ , in agreement with the fact that  $P_{xx} - P_{yy} \propto \langle C_x^2 \rangle - \langle C_y^2 \rangle > 0$ . These two effects are obviously more pronounced for  $\alpha = 0.5$  than for  $\alpha = 0.9$ .

Figure 17 shows that an excellent agreement between the IHS and EHS distributions for an inelasticity  $\alpha = 0.9$  exists in the region of low and intermediate velocities, in consistency with the results displayed in Figs. 14–

16. For  $\alpha = 0.5$ , it is observed that the EHS distributions  $g_x^{(+)}(C_x)$ ,  $g_y^{(+)}(C_y)$ , and  $F(C)$  are more populated than the IHS ones in the regions  $-1 \lesssim C_x \lesssim 0$ ,  $-0.3 \lesssim C_y \lesssim 0$ , and  $C \lesssim 0.5$ , respectively. It is also interesting to note that, in the region of thermal velocities, the orientation-averaged distribution function  $F(C)$  is much less distorted with respect to the Maxwellian than the marginal distributions  $g_x^{(+)}(C_x)$  and  $g_y^{(+)}(C_y)$ , especially in the case  $\alpha = 0.9$ . Another important finding is that the BGK kinetic model, not only captures well

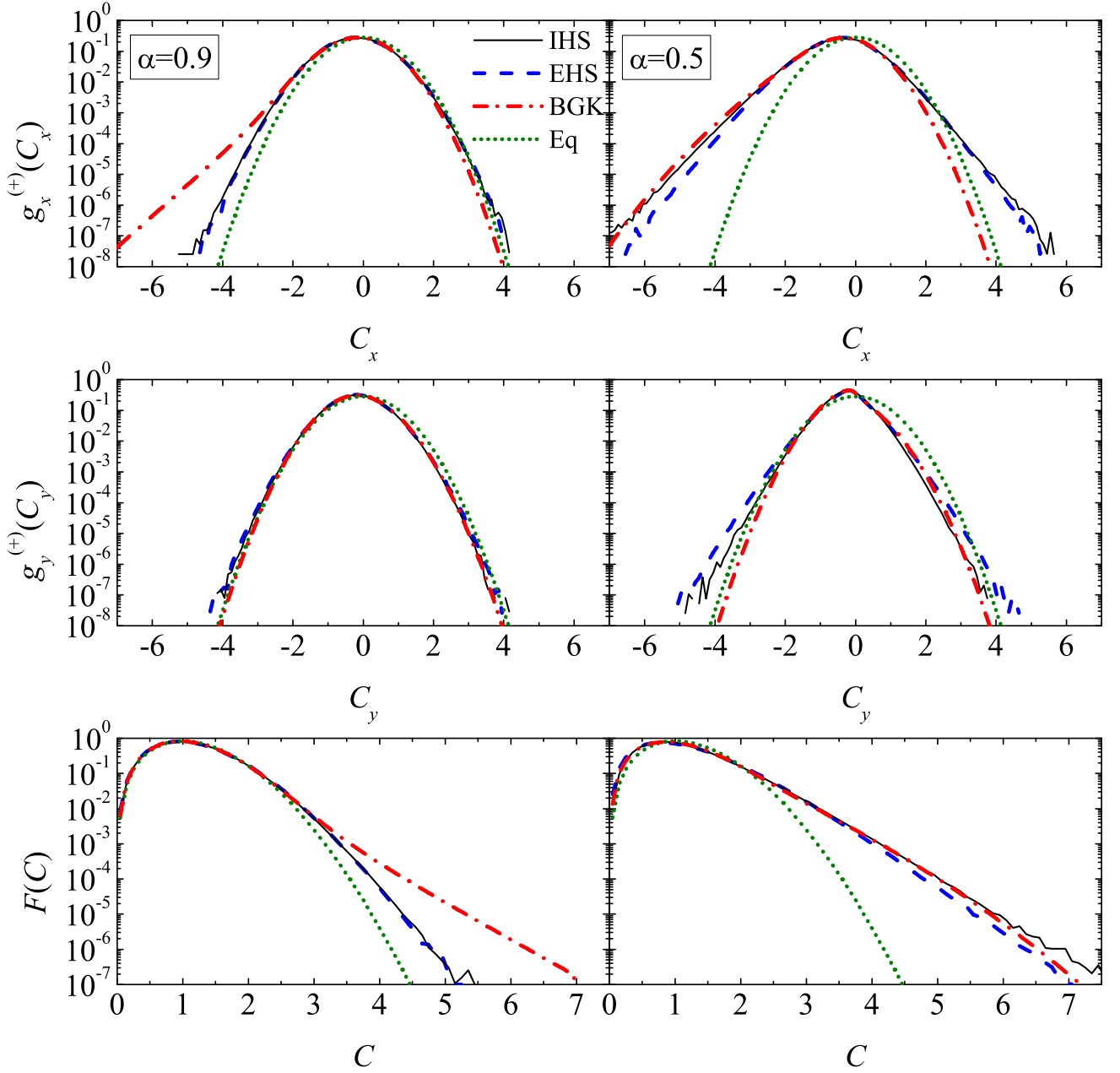


FIG. 18: (Color online) Logarithmic plots of the marginal velocity distribution functions  $g_x^{(+)}(C_x)$ ,  $g_y^{(+)}(C_y)$ , and  $F(C)$  for  $\alpha = 0.9$  (left panels) and  $\alpha = 0.5$  (right panels). The solid and dashed lines represent simulation results for IHS and EHS, respectively, the dash-dot lines are the BGK predictions, and the dotted lines are the (local) equilibrium distributions.

“global” or average properties, such as the hydrodynamic quantities (cf. Figs. 14–16), but also the “local” details of the velocity distribution function.

The logarithmic scale employed in Fig. 18 has been chosen to reveal the high-velocity tails of the distributions. We observe an overpopulation of both tails of  $g_x^{(+)}$ , especially at  $\alpha = 0.5$ . In the case of  $g_y^{(+)}$ , however, the overpopulation seems to affect the tail  $C_y < 0$  only. The high-energy overpopulation is clearly apparent in the distribution of the magnitude of the velocity,  $F(C)$ . In a recent paper, Bobylev et al. [53] have proven that

$\ln F(C) \sim -C^\mu$ , with  $\mu \geq 1$ , for asymptotically large velocities in the USF. Although it is not clear whether our simulation data have reached the high-velocity regime where the asymptotic law  $\ln F(C) \sim -C^\mu$  dominates, the bottom panels of Fig. 18 seem to be consistent with this law with  $\mu \simeq 1$ .

The comments in the preceding paragraph apply equally to IHS and EHS. As a matter of fact, the simulation data for both systems in the case  $\alpha = 0.9$  are hardly distinguishable for that value of  $\alpha$ . In the case  $\alpha = 0.5$ , however, the high-velocity values of  $g_x^{(+)}(C_x)$

and  $F(C)$  are larger for IHS than for EHS, while the opposite happens for the high-velocity values of  $g_y^{(+)}(C_y)$ . As for the BGK distribution function, it cannot be expected to be accurate beyond the domain of thermal velocities. This is confirmed by Fig. 18, where we can observe that at  $\alpha = 0.9$  the BGK model strongly exaggerates the high-velocity overpopulation effects of  $g_x^{(+)}(C_x)$  and  $F(C)$ . This produces too large a value of the sixth cumulant  $-a_3$ , as observed in Fig. 16. On the other hand, at  $\alpha = 0.5$  the BGK value of  $-a_3$  agrees by accident with that of the IHS system and this explains why in that case the overpopulated tail predicted by the BGK model agrees well with that of the IHS system. Nevertheless, the tail of  $g_x^{(+)}(C_x)$  for  $C_x > 0$  as well as that of  $g_y^{(+)}(C_y)$  for  $C_y < 0$  are strongly underestimated by the BGK model at  $\alpha = 0.5$ .

For the sake of clarity, we have not included in the right panels of Figs. 17 and 18 the curves corresponding to our simulations of the EHS system with  $\alpha = 0.5$  and a friction constant  $\gamma = \frac{1}{2}\zeta_0 \langle V_{12}^3 \rangle / \langle V_{12}^3 \rangle_0$ . In any case, the results are very close to those corresponding to the friction constant  $\gamma = \frac{1}{2}\zeta_0$ . This shows that the main quantitative differences between highly dissipative IHS and EHS systems, in particular the high-velocity tails, are intrinsic to the different dynamics of both systems and so they are not avoided by a fine-tuning of the drag force acting on the elastic particles.

## VI. CONCLUSIONS

In this paper we have dealt with the main nonequilibrium properties of two classes of dissipative gases subject to the so-called simple or uniform shear flow (USF). In the first class, the system is made of inelastic hard spheres (IHS) with a constant coefficient of restitution  $\alpha < 1$ . The inelasticity of collisions provides an internal energy sink, characterized by a cooling rate  $\zeta$ . In the second class, the particles are elastic hard spheres (EHS) under the action of a drag force, so that the energy sink is now external and characterized by a friction coefficient  $\gamma$ . At a given value of  $\alpha$ , some of the basic properties of the Boltzmann equation for the IHS gas are formally similar to those for the (frictional) EHS gas [4] if (i) the friction coefficient is chosen as a function of the local density and temperature,  $\gamma = \frac{1}{2}\zeta_0 \propto nT^{1/2}(1 - \alpha^2)$ , and (ii) the collision rate of the EHS gas is  $\beta(\alpha) = \frac{1}{2}(1 + \alpha)$  times the collision rate of the IHS gas under the same conditions. The boundary conditions of the USF state provides an energy source (viscous heating) that competes with the energy dissipation (either collisional or frictional), until a steady state is eventually reached, resulting from the balance between both effects.

The two main points we have intended to address in this paper are the following ones. On the one hand, we wanted to perform an extensive study of the physical properties of dissipative gases under USF, for both the

transient and the steady states. While the USF state has been widely considered in the literature of granular fluids, some of its relevant aspects (hydrodynamic transient stage, cumulants, high-velocity tail, ...) have received little attention. As a second point, taking the USF as a paradigmatic and conceptually simple nonequilibrium state, we were interested in elucidating to what extent the EHS gas mimics the physical properties of the genuine IHS gas. To meet these goals, we have carried out computer simulations by the DSMC method on both classes of systems for ten values of the coefficient of restitution ( $\alpha = 0.5-0.95$  with a step  $\Delta\alpha = 0.05$ ) and two values of the shear rate ( $a = 4/\tau^0$  and  $a = 0.1/\tau^0$ ). Below we summarize the main conclusions derived from our study.

The duration of the transient period, when measured by the number of collisions per particle ( $s$ ), is hardly dependent on the imposed shear rate  $a$  or on the initial state, but strongly depends on the coefficient of restitution  $\alpha$ . The larger the dissipation, the smaller the number of collisions needed to reach the steady state. For instance,  $s \simeq 40$  at  $\alpha = 0.9$ , while  $s \simeq 20$  at  $\alpha = 0.5$ . Nevertheless, when the duration is measured by an external clock (for instance, in units of the initial mean free time), it becomes weakly dependent on  $\alpha$  but strongly dependent on  $a$ : the smaller the imposed shear rate, the longer the transient period.

The evolution toward the steady state proceeds in two stages. The first (kinetic) stage depends heavily on the initial preparation of the system and lasts a few collisions per particle. This is followed by a much slower hydrodynamic regime that becomes less and less dependent on the initial state. Once conveniently scaled with the thermal speed  $v_0(t) = \sqrt{2T(t)/m}$ , the velocity distribution function in the hydrodynamic regime depends on time through the reduced velocity  $\mathbf{C}(t) = \mathbf{V}/v_0(t)$  and the reduced shear rate  $a^*(t) \propto a/\sqrt{T(t)}$  only [6]. In particular, at a given value of  $\alpha$ , the (reduced) nonlinear shear viscosity  $\eta^*(a^*)$  moves on a certain rheological curve, the steady-state value  $\eta_s^* = \eta^*(a_s^*)$  representing just one point. This point splits the curve  $\eta^*(a^*)$  into two branches. The branch  $a^* \leq a_s^*$  is accessible from initial states such that the dissipative cooling dominates over the viscous heating, so that  $T(t)$  decreases and  $a^*(t)$  increases during the transient period. Conversely, the branch  $a^* \geq a_s^*$  corresponds to initial states where the viscous heating dominates, so that  $T(t)$  increases and  $a^*(t)$  decreases, until the steady state is reached.

The actual number of collisions per particle  $s(t)$  is slightly smaller than the local equilibrium estimate  $s_0(t)$ . This indicates that  $\langle V \rangle < \langle V \rangle_0$ , whereas  $\langle V^2 \rangle = \langle V^2 \rangle_0 = 3T(t)/m$  by definition. The inequality  $\langle V \rangle < \langle V \rangle_0$  is consistent with an underpopulation (with respect to the local equilibrium distribution) for moderate velocities that must be compensated by a high-velocity overpopulation. This qualitative reasoning is confirmed by the inequalities  $\langle V_{12}^3 \rangle > \langle V_{12}^3 \rangle_0$ ,  $\langle V^4 \rangle > \langle V^4 \rangle_0$ , and  $\langle V^6 \rangle > \langle V^6 \rangle_0$  observed in the simulations. In addition to these effects, the shearing motion induces a strong anisotropy in the nor-

mal stresses, namely  $P_{xx}(t) > nT(t) > P_{zz}(t) \gtrsim P_{yy}(t)$ . In other words, a breakdown of the energy equipartition occurs, whereby the “temperature” associated with the degree of freedom parallel to the fluid motion is significantly larger than that associated with the other two degrees of freedom, as already observed in previous studies [14, 15, 16, 17, 20, 22, 24, 26, 28, 30, 36, 38].

We have paid special attention to the properties of the steady state, which is intrinsically independent of the imposed shear rate and of the initial state. As expected, the distortion from the local equilibrium state (as measured by the shear stress, the normal stress differences, the cumulants, ...) increases with the dissipation. This distortion is made quite apparent by the shapes of the steady-state (marginal) velocity distributions defined by Eqs. (3.18)–(3.20). In particular, the high-velocity tails of  $g_x^{(+)}(C_x)$  and  $F(C)$  seem to be consistent with an exponential overpopulation.

All the above comments apply equally well to the IHS and EHS gases. Therefore, the main nonequilibrium and transport properties of a true IHS gas in the USF state are satisfactorily mimicked by an “equivalent” EHS gas. If one focus on the basic properties (say the steady-state reduced shear rate  $a_s^*$ , shear stress  $P_{xy,s}/nT_s$ , or second cumulant  $a_2$ ) it is almost impossible to distinguish the EHS values from the IHS ones if  $\alpha \gtrsim 0.7$ , the differences still being relatively small if  $\alpha \lesssim 0.7$ . We have observed that  $\langle V_{12}^3 \rangle / \langle V_{12}^3 \rangle_0$  and  $a_2$  are in the EHS system slightly larger than in the IHS system if  $\alpha \gtrsim 0.7$ , while the opposite happens if  $\alpha \lesssim 0.7$ ; this is analogous to what happens in the homogeneous cooling state and in the white-noise heated state, in which cases the EHS distribution is exactly a Maxwellian. It is interesting to note that, even at  $\alpha = 0.5$ , the full hydrodynamic curve  $\eta^*(a^*)$  coincides for both systems, except that the location of the steady-state point  $\eta_s^* = \eta^*(a_s^*)$  slightly changes. More delicate quantities (such as the normal stress differences or the sixth cumulant) keep being practically the same in both systems if  $\alpha \gtrsim 0.85$ . Even at the level of the velocity distribution function itself, the EHS and IHS curves practically overlap (at least for the domain of velocities  $C \lesssim 6$  accessible to our computer simulations) at a coefficient of restitution as realistic as  $\alpha = 0.9$ . At  $\alpha = 0.5$ , however, the distribution functions  $g_x^{(+)}(C_x)$  and  $F(C)$  of the IHS system exhibit a visibly larger high-velocity overpopulation than those of the EHS system.

As said above, in the EHS systems we have chosen the friction coefficient as  $\gamma = \frac{1}{2}\zeta_0 \propto nT^{1/2}(1 - \alpha^2)$ , so that it is a functional of the distribution function only through the local density and temperature and, moreover, its dependence on  $\alpha$  is explicit. Given that the true cooling rate is slightly larger than the local equilibrium estimate, i.e.,  $\zeta/\zeta_0 = \langle V_{12}^3 \rangle / \langle V_{12}^3 \rangle_0 > 1$ , the imitation of the inelastic cooling rate by the EHS is not perfect. Therefore, one might reasonably expect that the discrepancies between the EHS and IHS results would diminish if the friction coefficient were taken as  $\gamma = \frac{1}{2}\zeta_0 \langle V_{12}^3 \rangle / \langle V_{12}^3 \rangle_0$ . To test this expectation, we have performed complementary simula-

tions of the EHS system with this more refined value of  $\gamma$  in the case of highest dissipation, i.e.,  $\alpha = 0.5$ . The results show that, whenever the former agreement between EHS and IHS was fair, the new agreement is generally even better. However, those quantities (such as the normal stress difference  $P_{zz} - P_{yy}$  and the sixth cumulant  $a_3$ ) that turned out to be especially sensitive to the dissipation mechanism (collisional inelasticity versus external friction) are practically unaffected by the new choice of  $\gamma$ . Moreover, the high-velocity tails of both versions of the EHS gas are practically the same, being both smaller than the IHS tail. Therefore, the (subtle) discrepancies between the IHS and EHS systems in cases of high dissipation (say  $\alpha \lesssim 0.7$ ) seem to be intrinsic to their distinct dynamics. Taking this into account, there is no practical reason to propose for the drag force acting on the EHS a friction coefficient different from the local equilibrium value  $\gamma = \frac{1}{2}\zeta_0$ . Concerning the collision rate coefficient  $\beta(\alpha)$ , the choice  $\beta(\alpha) = \frac{1}{2}(1 + \alpha)$  is recommended by criteria of simplicity and consistency with the cases of mixtures and dense gases [4]. Moreover, we have checked (not shown in this paper) that an alternative choice, namely  $\beta(\alpha) = \frac{1}{6}(1 + \alpha)(2 + \alpha)$ , although reproducing well the Navier–Stokes shear viscosity [4], provides results for the nonlinear shear viscosity in worse agreement with the IHS ones than those reported here with  $\beta(\alpha) = \frac{1}{2}(1 + \alpha)$ .

The (approximate) equivalence IHS $\leftrightarrow$ EHS can be used to transfer to granular gases part of the expertise accumulated for a long time on the kinetic theory of elastic particles. In particular, the celebrated Bhatnagar–Gross–Krook (BGK) kinetic model of the Boltzmann equation can be readily extended to granular gases [4, 7]. In this paper we have compared the solution of the BGK model for USF [4, 6, 26] with the simulation data. While it is generally believed that the BGK model would be accurate only for states near equilibrium and/or in the quasi-elastic limit, our results show that, despite its simplicity, the model succeeds in capturing quantitatively the evolution and steady-state values of the main transport properties (temperature, shear stress, and normal stress difference  $P_{xx} - P_{yy}$ ) and even of the fourth cumulant  $a_2$ . However, the small nonzero difference  $P_{zz} - P_{yy}$  is not accounted for by the BGK model and the sixth cumulant  $a_3$  agrees with the simulation data at a qualitative level only. All of this is consistent with the observation that the BGK velocity distribution function is reliable in the thermal region ( $C \lesssim 2$ ), but not in the high-velocity domain.

In summary, we conclude that the solutions of the Boltzmann equations for IHS are very similar to those for EHS (in the latter case with a smaller collision rate and under the action of an adequate drag force). Thus the temporal evolution toward the steady state and the properties of the latter are mainly governed by the common feature of energy dissipation, without any significant influence of the detailed mechanism behind it. Only for very high dissipation (say  $\alpha \lesssim 0.7$ ) and for properties probing the velocity domain beyond the thermal region,

does the IHS system imprint its signature and distinguish from the “disguised” EHS system. In this paper we have restricted ourselves to the USF, but we plan to perform a similar comparison in other states, especially in those where the heat flux, rather than the pressure tensor, is the relevant quantity. We will also undertake a parallel study in the case of dilute mixtures, as well as in the case of dense gases (complemented by molecular dynamics simulations), following the schemes discussed in the preceding paper [4].

## Acknowledgments

We are grateful to V. Garzó for a critical reading of the manuscript. Partial support from the Ministerio de Educación y Ciencia (Spain) through grant No. FIS2004-01399 (partially financed by FEDER funds) is gratefully acknowledged. A.A. is grateful to the Fundación Ramón Areces (Spain) for a predoctoral fellowship.

- 
- [1] A. Goldshtein and M. Shapiro, *J. Fluid Mech.* **282**, 75 (1995).
- [2] J. J. Brey, J. W. Dufty, and A. Santos, *J. Stat. Phys.* **87**, 1051 (1997).
- [3] T. P. C. van Noije and M. H. Ernst, in *Granular Gases*, edited by T. Pöschel and S. Luding, Lecture Notes in Physics, Vol. 564 (Springer-Verlag, Berlin, 2001), pp. 3–30.
- [4] A. Santos and A. Astillero, “System of elastic hard spheres which mimics the transport properties of a granular gas;” arXiv: cond-mat/0405252.
- [5] I. Goldhirsch, *Annu. Rev. Fluid Mech.* **35**, 267 (2003).
- [6] A. Santos, V. Garzó, and J. W. Dufty, *Phys. Rev. E* **69**, 061303 (2004).
- [7] J. J. Brey, J. W. Dufty, and A. Santos, *J. Stat. Phys.* **97**, 281 (1999). Note a misprint in Eq. (C.11): The right-hand sides of the two equations should be multiplied by  $(d-1)(d+2)/2$  and  $d$ , respectively.
- [8] J. J. Brey, J. W. Dufty, C. S. Kim, and A. Santos, *Phys. Rev. E* **58**, 4638 (1998).
- [9] S. Chapman and T. G. Cowling, *The Mathematical Theory of Nonuniform Gases* (Cambridge University Press, Cambridge, 1970).
- [10] Note that, strictly speaking, the relationships  $\lambda' = \lambda/\beta$  and  $\tau' = \tau/\beta$  only hold if the EHS and IHS gases have the same density and temperature.
- [11] This must be distinguished from a system of *rough* spheres with a coefficient of normal restitution  $\alpha = 1$ . The latter system has been considered, for instance, by S. J. Moon, J. B. Swift, and H. L. Swinney, *Phys. Rev. E* **69**, 011301 (2004).
- [12] For a preliminary report of this research, see A. Astillero and A. Santos, “A granular fluid modeled as a driven system of elastic hard spheres,” in *The Physics of Complex Systems (New Advances and Perspectives)*, edited by F. Mallamace and H. E. Stanley (IOS Press, Amsterdam, 2004), pp. 475–480; arXiv: cond-mat/0309220.
- [13] C. K. K. Lun, S. B. Savage, D. J. Jeffrey, and N. Chepurniy, *J. Fluid Mech.* **140**, 223 (1984).
- [14] C. S. Campbell and A. Gong, *J. Fluid Mech.* **164**, 107 (1986).
- [15] O. R. Walton and R. L. Braun, *J. Rheol.* **30**, 949 (1986); *Acta Mech.* **63**, 73 (1986).
- [16] J. T. Jenkins and M. W. Richman, *J. Fluid Mech.* **192**, 313 (1988).
- [17] C. S. Campbell, *J. Fluid Mech.* **203**, 449 (1989).
- [18] C. S. Campbell, *Annu. Rev. Fluid Mech.* **22**, 57 (1990).
- [19] S. B. Savage, *J. Fluid Mech.* **241**, 109 (1992).
- [20] M. A. Hopkins and H. H. Shen, *J. Fluid Mech.* **244**, 477 (1992).
- [21] P. J. Schmid and H. K. Kytömaa, *J. Fluid Mech.* **264**, 255 (1994).
- [22] C. K. K. Lun and A. A. Bent, *J. Fluid Mech.* **258**, 335 (1994).
- [23] I. Goldhirsch and M. L. Tan, *Phys. Fluids* **8**, 1752 (1996).
- [24] N. Sela, I. Goldhirsch, and S. H. Noskowitz, *Phys. Fluids* **8**, 2337 (1996).
- [25] C. S. Campbell, *J. Fluid Mech.* **348**, 85 (1997).
- [26] J. J. Brey, M. J. Ruiz-Montero, and F. Moreno, *Phys. Rev. E* **55**, 2846 (1997).
- [27] C.-S. Chou and M. W. Richman, *Physica A* **259**, 430 (1998); C.-S. Chou, *ibid.* **287**, 127 (2000); **290**, 341 (2001).
- [28] J. M. Montanero, V. Garzó, A. Santos, and J. J. Brey, *J. Fluid Mech.* **389**, 391 (1999).
- [29] V. Kumaran, *Physica A* **275**, 483 (2000); **284**, 246 (2000); **293**, 385 (2001).
- [30] A. Frezzotti, *Physica A* **278**, 161 (2000).
- [31] C. Cercignani, *J. Stat. Phys.* **102**, 1407 (2001).
- [32] M. Alam and C. M. Hrenya, *Phys. Rev. E* **63**, 061308 (2001).
- [33] R. Clelland and C. M. Hrenya, *Phys. Rev. E* **65**, 031301 (2002).
- [34] V. Garzó, *Phys. Rev. E* **66**, 021308 (2002); *J. Stat. Phys.* **112**, 657 (2003).
- [35] J. M. Montanero and V. Garzó, *Physica A* **310**, 17 (2002); *Mol. Sim.* **29**, 357 (2003).
- [36] A. V. Bobylev, M. Groppi, and G. Spiga, *Eur. J. Mech. B/Fluids* **21**, 91 (2002).
- [37] V. Garzó and J. M. Montanero, *Phys. Rev. E* **68**, 041302 (2003).
- [38] M. Alam and S. Luding, *J. Fluid Mech.* **476**, 69 (2003); *Phys. Fluids* **15**, 2298 (2003).
- [39] J. F. Lutsko, *Phys. Rev. E* **70**, 061101 (2004).
- [40] J. M. Montanero, V. Garzó, M. Alam, and S. Luding, “Rheology of granular mixtures under uniform shear flow: Enskog kinetic theory versus molecular dynamics simulations,” arXiv: cond-mat/0411548.
- [41] See, for instance, V. Garzó and A. Santos, *Kinetic Theory of Gases in Shear Flows. Nonlinear Transport* (Kluwer Academic Publishers, Dordrecht, 2003), Chaps. 2–4, and references therein.
- [42] M. Tij, E. Tahiri, J. M. Montanero, V. Garzó, A. Santos, and J. W. Dufty, *J. Stat. Phys.* **103**, 1035 (2001).
- [43] A. W. Lees and S. F. Edwards, *J. Phys. C* **5**, 1921 (1972).
- [44] J. W. Dufty, A. Santos, J. J. Brey, and R. F. Rodríguez, *Phys. Rev. A* **33**, 459 (1986).
- [45] To avoid confusion in the notation, we use the superscript

- 0 to refer to initial quantities (e.g.,  $T^0$ ), while we usually employ the subscript 0 to denote local equilibrium quantities (e.g.,  $\zeta_0$ ).
- [46] G. Bird, *Molecular Gas Dynamics and the Direct Simulation of Gas Flows* (Clarendon, Oxford, 1994).
- [47] F. J. Alexander and A. L. Garcia, *Comp. Phys.* **11**, 588 (1997).
- [48] For an extension of the DSMC method to the Enskog equation, see J. M. Montanero and A. Santos, *Phys. Rev. E* **54**, 438 (1996); *Phys. Fluids* **9**, 2057 (1997); A. Frezzotti, *ibid.* **9**, 1329 (1997).
- [49] V. Garzó, “Transport coefficients for a granular gas around uniform shear flow,” arXiv: cond-mat/0506013.
- [50] P. L. Bhatnagar, E. P. Gross, and M. Krook, *Phys. Rev.* **94**, 511 (1954); P. Welander, *Arkiv. Fysik* **7**, 507 (1954).
- [51] T. P. C. van Noije and M. H. Ernst, *Gran. Matt.* **1**, 57 (1998).
- [52] J. M. Montanero and A. Santos, *Gran. Matt.* **2**, 53 (2000).
- [53] A. V. Bobylev, I. M. Gamba, and V. A. Panferov, *J. Stat. Phys.* **116**, 1651 (2004).